

High accuracy power series method for solving scalar, vector, and inhomogeneous nonlinear Schrödinger equations

L. Al Sakkaf and U. Al Khawaja

*Department of Physics, United Arab Emirates University,
P.O. Box 15551, Al-Ain, United Arab Emirates*

We develop a high accuracy power series method for solving partial differential equations with emphasis on the nonlinear Schrödinger equations. The accuracy and computing speed can be systematically and arbitrarily increased to orders of magnitude larger than those of other methods. Machine precision accuracy can be easily reached and sustained for long evolution times within rather short computing time. In-depth analysis and characterisation for all sources of error are performed by comparing the numerical solutions with the exact analytical ones. Exact and approximate boundary conditions are considered and shown to minimise errors for solutions with finite background. The method is extended to cases with external potentials and coupled nonlinear Schrödinger equations.

PACS numbers:

I. INTRODUCTION

The nonlinear Schrödinger equation (NLSE) is truly a universal equation as it describes major fields such as Bose-Einstein condensation [1], nonlinear optics [2], ocean waves [3], and many others [4–6]. This has stimulated extensive interest in its analytical [7] and numerical solutions [8–10, 12–19]. Over decades, knowledge about its analytical solutions has accumulated such that it is now rare to find a new solution [7]. A plethora of numerical methods have also been developed to solve its nonlinear initial value problem, such as the incoherent scattering of solitons with each other or the scattering of solitons by external potentials. Some solutions demand higher accuracy than others such as dark solitons or vortex excitations since they have nonzero background or extend over the whole system, which warrants accurate account of the boundary conditions. Some other solutions have a fast time evolution or high curvature such as the coalescing soliton molecule or Peregrine soliton. This kind of solutions requires accurate integrator of the time derivative. Many of the numerical methods developed already solve these problems, but there is always a demand on increasing accuracy and decreasing computing time and memory cost, particularly for large system sizes or long evolution times. Explicit methods solving the NLSE can be categorised into two major classes, namely spectral methods and finite difference methods [10], in addition to other methods using, for instance, quadrature discretisation [20–23] or wavelet expansion [17].

Here, we present a method that can systematically increase the accuracy in both the spacial and temporal axes. For the temporal evolution, we use an iterative power series method that we have developed previously for ordinary differential equations [24] and applied later to fluid flow [25]. The accuracy in the time evolution increases with the maximum power in the time power series, s . For the spacial part, we use a p -point stencil to discretise the second derivative, where $p \geq 3$ is a positive odd integer. The accuracy can be systematically increased by increasing s and p . The method requires the knowledge of the initial profile and its boundary conditions. While an arbitrary initial profile can be used, using an exact solution as the initial profile, makes it possible to calculate the evolution of error and compare it with other numerical methods. The exact solutions we consider here include: moving bright soliton, moving dark soliton, Peregrine soliton, and soliton molecule. For all of these solutions, our method shows a remarkable performance with accuracy that can reach the machine precision for a long evolution time in a rather short computing time.

We perform an extensive analysis of the different sources of error originating from spacial discretisation, temporal discretisation, and boundary conditions. We then compare our method with two methods representing the finite difference and spectral methods. Among the many finite difference methods, the so-called generalized finite-difference time-domain (G-FDTD) method [8–10, 26] is superior in its high accuracy. Based on our analysis and understanding of the interplay between the different sources of error, the present method makes significant enhancements on the G-FDTD method in terms of accuracy or computing time. Specifically, we enhance on the time stepping method, make no approximations in the derivation of the recursion relations of the time power series, and account for the evolution of boundary points exactly, even when the initial profile is not an exact solution. Furthermore, we show that using the so-called constant wave (CW) exact solution to compute approximate boundary conditions is in most cases as good as using the exact ones for localised solutions over a uniform background, as long as the localisation does not come close to the boundaries within the considered time domain. This is shown with a detailed comparison performed for the bright and dark soliton solutions. For the spectral methods, we compare with the Fourier split-step (SS) method [11], where we show that the present method is significantly more accurate and faster.

The method is extended to inhomogeneous NLSE and applied to the nonintegrable case of a bright soliton scattered by a reflectionless potential well. An accurate account to the quantum reflection effect and to the value of the critical speed [27–29] are obtained, where extremely high accuracy is required when the soliton speed is close enough to the critical speed. We show that other numerical methods lead to the wrong outcome (reflection instead of transmission), while the present method captures the correct behaviour right at its lowest level of accuracy ($p = 3$).

Finally, the method is generalised to the case of two coupled NLSEs, known as the Manakov system, from which the evolution of the dark-bright soliton is calculated accurately.

The rest of the paper is organised as follows. In Section II, we present the proposed theoretical framework and algorithm of the method. In Section III, we perform a detailed analysis of the different sources of error and characterize them in terms of s and p . In Section IV, we compare the accuracy and CPU run time with other methods. In Section V, we consider the Peregrine soliton and soliton molecule as initial profiles. In Section VI, we extend the method to NLSE with an external potential. In Section VII, we generalize to the two-coupled NLSE or Manakov system. We end in Section VIII with a summary and outlook for future work.

II. NUMERICAL METHOD

While emphasis will be on the NLSE, the method we describe below can be modified to solve other evolution equations. The fundamental NLSE can be written in dimensionless form as

$$i \frac{\partial}{\partial t} \psi(x, t) + g_1 \frac{\partial^2}{\partial x^2} \psi(x, t) + g_2 |\psi(x, t)|^2 \psi(x, t) = 0, \quad (1)$$

where $\psi(x, t)$ is a complex function, g_1 and g_2 are arbitrary real constants representing the strength of dispersion and nonlinear terms, respectively. In nonlinear optics, the NLSE describes the propagation of pulses in nonlinear media. In such a context, the dispersion term corresponds to the group velocity dispersion (GVD), which, depending on the sign of g_1 , compresses or spreads out the pulse, while the nonlinear term corresponds to what is known as the Kerr effect, which describes the modulation of the refractive index of the medium as a response to the propagating light pulse.

The statement of the problem is defined as follows: Given an arbitrary initial profile $\psi_0(x) = u_0(x) + i v_0(x)$ and boundary conditions on $\psi(\pm L/2, t)$ at the edges of the spacial domain, $x = \pm L/2$, what is the time evolution of $\psi_0(x)$ governed by the NLSE, Eq. (1)? The method presented

here solves this nonlinear initial value problem, which is described briefly as follows. The solution is expanded in a power series in time as $\psi(x, t) = c_0(x) + c_1(x)t + c_2(x)t^2 + \dots + c_s(x)t^s$, where s is a positive integer. Recursion relations for the coefficients $c_l(x)$, $l > 0$, will be given in terms of the initial profile $c_0(x)$ upon substituting in (1). The spacial domain is discretised using a p -point stencil to replace the second derivative, where p is an odd integer ≥ 3 . As a result, the first and last $(p - 1)/2$ points of the spacial grid can not be determined by the recursion relations and need to be determined from boundary conditions. For the class of solutions which we consider here, namely a localised profile over a uniform background, the CW exact solution may be used to accurately calculate these boundary conditions. The schematic figure, Fig. 1, depicts the picture just described. Accuracy in the method is thus determined by three factors: i) the order of the time power series s , with error $\propto \Delta t^{s+1}$, where Δt is the small discretisation in the time domain, ii) the number of points in the p -point formula approximating the second spacial derivative with error $\propto \Delta x^{p-1}$, where Δx is the small discretisation in the spatial domain, iii) the accuracy in the boundary conditions, namely how accurately does the CW solution represent the evolution of the first and last $(p - 1)/2$ boundary points.

We use in this work values of $s \leq 4$ and mostly $p \leq 23$. It turns out that very high accuracy which can easily reach machine precision is accessible for a long evolution time but still with a short run time. In the following, the method is described in detail.

A. Time evolution and recursion relations

Without loss of generality, we write the general solution in the cartesian complex form of

$$\psi(x, t) = u(x, t) + i v(x, t), \quad (2)$$

where $u(x, t)$ and $v(x, t)$ being real functions. Inserting in (1), generates the following two equations from the real and imaginary parts

$$g_1 \frac{\partial^2}{\partial x^2} u(x, t) + g_2 [u^2(x, t) + v^2(x, t)] u(x, t) - \frac{\partial}{\partial t} v(x, t) = 0, \quad (3)$$

$$g_1 \frac{\partial^2}{\partial x^2} v(x, t) + g_2 [u^2(x, t) + v^2(x, t)] v(x, t) + \frac{\partial}{\partial t} u(x, t) = 0. \quad (4)$$

To integrate the time operator, we expand the solutions $u(x, t)$ and $v(x, t)$ in powers of the small discretization of the time domain, Δt , as follows

$$u(x, t) = \sum_{l=0}^s a_l(x) \Delta t^l, \quad (5)$$

$$v(x, t) = \sum_{l=0}^s b_l(x) \Delta t^l, \quad (6)$$

where s is a positive nonzero integer and the function coefficients are defined by

$$a_l(x) = \frac{1}{l!} \frac{\partial^l}{\partial t^l} u(x, t)|_{t=0}, \quad (7)$$

$$b_l(x) = \frac{1}{l!} \frac{\partial^l}{\partial t^l} v(x, t)|_{t=0}. \quad (8)$$

The initial profile is given by $\psi_0(x) = a_0(x) + i v_0(x)$. We refer to the maximum power of this expansion, s , as the ‘‘order’’. The order is one of two factors that can be used to increase the

accuracy of the method. By terminating the power series at s , an error

$$\begin{aligned} error_s &= \mathcal{O}\left(\frac{\Delta t^{s+1}}{(s+1)!} \frac{\partial^{s+1}}{\partial t^{s+1}} u(x, t)|_{t=0}\right) \\ &= \mathcal{O}\left(\frac{\Delta t^{s+1}}{(s+1)!} \frac{\partial^{s+1}}{\partial t^{s+1}} v(x, t)|_{t=0}\right) \end{aligned} \quad (9)$$

is introduced. To proceed, we need to specify the value of s , which we choose as $s = 4$. The expansions (5) and (6) then read

$$u(x, t) = a_0(x) + a_1(x)t + a_2(x)t^2 + a_3(x)t^3 + a_4(x)t^4, \quad (10)$$

$$v(x, t) = b_0(x) + b_1(x)t + b_2(x)t^2 + b_3(x)t^3 + b_4(x)t^4. \quad (11)$$

Substituting back into (3) and (4), recursion relations are obtained by equating the coefficients of Δt^i , $i = 0, 1, 2, 3$ to zero, as follows

$$a_1 = -g_2 a_0^2 b_0 - g_2 b_0^3 - g_1 b_0'', \quad (12)$$

$$a_2 = \frac{1}{2} [-2g_2 a_0 a_1 b_0 - g_2 a_0^2 b_1 - 3g_2 b_0^2 b_1 - g_1 b_1''], \quad (13)$$

$$\begin{aligned} a_3 &= \frac{1}{3} [-g_2 a_1^2 b_0 - 2g_2 a_0 a_2 b_0 - 2g_2 a_0 a_1 b_1 - 3g_2 b_0 b_1^2 \\ &\quad - g_2 a_0^2 b_2 - 3g_2 b_0^2 b_2 - g_1 b_2''], \end{aligned} \quad (14)$$

$$\begin{aligned} a_4 &= \frac{1}{4} [-g_2 a_1^2 b_1 - g_2 b_1^3 - 2g_2 a_0 a_3 b_0 - 2g_2 a_0 a_2 b_1 - 6g_2 b_0 b_1 b_2 \\ &\quad - 2g_2 a_1 a_2 b_0 - 2g_1 a_1 a_0 b_2 - g_2 a_0^2 b_3 - 3g_2 b_0^2 b_3 - g_1 b_3''], \end{aligned} \quad (15)$$

$$b_1 = g_2 a_0 b_0^2 + g_2 a_0^3 + g_1 a_0'', \quad (16)$$

$$b_2 = \frac{1}{2} [2g_2 a_0 b_0 b_1 + g_2 b_0^2 a_1 + 3g_2 a_0^2 a_1 + g_1 a_1''], \quad (17)$$

$$\begin{aligned} b_3 &= \frac{1}{3} [g_2 a_0 b_1^2 + 2g_2 a_0 b_2 b_0 + 2g_2 a_1 b_0 b_1 + 3g_2 a_0 a_1^2 \\ &\quad + g_2 a_2 b_0^2 + 3g_2 a_0^2 a_2 + g_1 a_2''], \end{aligned} \quad (18)$$

$$\begin{aligned} b_4 &= \frac{1}{4} [g_2 a_1 b_1^2 + g_2 a_1^3 + 2g_2 a_0 b_3 b_0 + 2g_2 a_0 b_1 b_2 + 6g_2 a_0 a_1 a_2 \\ &\quad + 2g_2 a_1 b_2 b_0 + 2g_2 a_2 b_0 b_1 + g_2 b_0^2 a_3 + 3g_2 a_0^2 a_3 + g_1 a_3''], \end{aligned} \quad (19)$$

where we hid the x -dependence for convenience and $(\cdot)''$ denotes a second derivative with respect to x . The structure of the recursion relations is such that the l^{th} coefficient is determined by the $(l-1)^{\text{th}}$ coefficients and the second derivative of one of the $(l-1)^{\text{th}}$ coefficients. For instance, a_1 is given in terms of a_0 , b_0 , and b_0'' .

B. Spacial discretisation and boundary conditions

The spacial domain of size $[-L/2, L/2]$ is divided into a number n_x of spacial discretizations, $\Delta x = L/(n_x - 1)$ such that $x_i = -L/2 + (i-1) \times \Delta x$, $i = 1, 2, \dots, n_x$. The coefficients $a_{1-4}(x)$ and $b_{1-4}(x)$ are then discretized and denoted as a_{1-4}^i and b_{1-4}^i , respectively. The crucial point is how to discretize the second derivative of the coefficients. The lowest order discretization is given by the

three-central-point (Euler) formula $a''_{1-3}(x) = [a_{1-3}(x + \Delta x) + a_{1-3}(x - \Delta x) - 2a_{1-3}(x)] / \Delta x^2$, which in discretized form reads $a''_{1-3} = (a_{1-3}^{i+1} + a_{1-3}^{i-1} - 2a_{1-3}^i) / \Delta x^2$, and similarly for b''_{1-3} . Using the forward or backward formula would be as accurate as the central point formula, but the later is more convenient for clearly exhibiting the symmetry in the boundary conditions, as will be detailed below.

A major source of error is introduced by the discretization of the second derivative. For instance, in deriving the three-point formula, an error of order Δx^2 is introduced. For higher accuracy, we use the following formula for a general central point second derivative, denoted here and throughout as f''_p , of any odd number of points, p ,

$$f''_p \equiv \frac{d^2 f(x)}{dx^2} = \frac{1}{\Delta x^2 \sum_{j=1}^{(p-1)/2} C_j j^2} \times \sum_{j=1}^{(p-1)/2} C_j [f(x + j\Delta x) + f(x - j\Delta x) - 2f(x)] + \mathcal{O}\left(\frac{(\Delta x)^{p-1}}{(p+1)!} \frac{df^{p+1}(x)}{dx^{p+1}}\right), \quad (20)$$

where the p -dependent coefficients, C_j , are determined by an appropriate linear combination of the Taylor expansions of $f(x + j\Delta x)$, $j = \pm 1, \pm 2, \dots, \pm(p-1)/2$, which results in the following system

$$\sum_{j=1}^{(p-1)/2} C_j j^{2i} = 0 \quad (21)$$

for $i = 2, 3, \dots, (p-1)/2$, to be solved in terms of C_j . The last term in (20) gives the order of error introduced by this approximation to the second derivative. This error appears in the coefficients a_{1-4} and b_{1-4} of Eqs. (5) and (6). However, the dominant contribution will be from a_1 and b_1 since they are multiplied by Δt , while the rest of coefficients are multiplied by higher powers of Δt . Therefore, the second source of error in our method takes the form

$$error_p = \max \left[\Delta t \frac{\partial}{\partial t} \frac{(\Delta x)^{p-1}}{(p+1)!} \frac{\partial |\psi^{p+1}(x, t)|}{\partial x^{p+1}} \right]. \quad (22)$$

The detailed derivation of the p -point formulae is relegated to Appendix A together with explicit formulae for the cases $p = 5, \dots, 23$.

Using the p -point approximation to the second derivative, the coefficients a_{1-4}^i and b_{1-4}^i will be given in terms of a p -point stencil composed of $(p-1)/2$ points to the left and $(p-1)/2$ points to the right of the central point. Consequently, the recursion relations can only be used for points $x_{(p-1)/2} < x_i < x_{n_x - (p-1)/2}$, which excludes the first and last $(p-1)/2$ points from the grid. The evolution of these two sets of points needs to be determined by the boundary conditions. In practise, there are different possibilities to consider. In many situations, an exact solution of the fundamental NLSE, (1), is used as an initial profile such as the bright or dark soliton to be scattered by other solitons or by a potential. In this case, the initial profile is not an exact solution anymore but represents an accurate approximation near the edges of the spacial domain. For these situations, the boundary conditions can be calculated from (10) and (11) using $u(x, t)$ and $v(x, t)$ as the exact solution considered for the initial profile. In other situations, an arbitrary initial localised profile that is not an exact solution to (1) is used. Near the edges of the spacial domain, which are assumed to be sufficiently far from the localisation for all times, the solution decays to

a uniform background. The uniform background, namely the CW solution, is an exact solution to the fundamental NLSE, (1). Therefore, the evolution of the boundary points may be calculated from (10) and (11) using $u(x, t)$ and $v(x, t)$ as the CW solution. The advantage of using the CW solution over using exact solutions to calculate the evolution of the boundary points is that it applies to all localised initial profiles as long as the localisation is away from the edges. This is very practical since it means that we can evolve any initial profile without a priori knowledge of the full time evolution of the boundary points. Using an exact solution, on the other hand, has the advantage of analytic continuation allowing the localisation to cross the boundaries of the spacial domain. We have verified that for cases with evolution times long enough to perform realistic numerical experiments, using the CW leads to almost the same accuracy in the evolved profile as when the exact solution is used for the initial profile.

Based on the above, the evolution of the coefficients $a_l(x)$ and $b_l(x)$ for for the bulk of the grid, namely $1 + (p - 1)/2 \leq i \leq n_x - (p - 1)/2$, read in the discretised form

$$a_1^i = -g_2 ((a_0^i)^2 + (b_0^i)^2) b_0^i - \frac{g_1}{\Delta x^2} \sum_{j=1}^{(p-1)/2} \bar{C}_j \left[b_0^{i+j} + b_0^{i-j} - 2b_0^i \right], \quad (23)$$

$$b_1^i = g_2 ((a_0^i)^2 + (b_0^i)^2) a_0^i + \frac{g_1}{\Delta x^2} \sum_{j=1}^{(p-1)/2} \bar{C}_j \left[a_0^{i+j} + a_0^{i-j} - 2a_0^i \right], \quad (24)$$

where $\bar{C}_j = C_j / \sum_{j=1}^{(p-1)/2} C_j j^2$. Equations for the rest of coefficients, a_{2-4}^i and b_{2-4}^i , can similarly be obtained by discretising (13-15) and (17-19). The boundary points, $1 \leq i \leq (p - 1)/2$ and $n_x - (p - 1)/2 < i \leq n_x$, are calculated from the boundary condition as

$$a_l^i = \frac{1}{l!} \frac{\partial^l}{\partial t^l} u(x_i, t)|_{t=0}, \quad (25)$$

$$b_l^i = \frac{1}{l!} \frac{\partial^l}{\partial t^l} v(x_i, t)|_{t=0}, \quad (26)$$

where, $u(x_i, t)$ and $v(x_i, t)$ correspond to an exact solution of (1). They may correspond to the time-dependent localized solution from which the initial profile is used. Alternatively, they may be the CW solution that the initial profile approaches at the boundaries. For the bright soliton, the CW solution that describes the asymptotes at the boundary is zero. Therefore, for this special case, all coefficients a_{1-4}^i and b_{1-4}^i can be set to zero at the boundary points defined above. This saves considerably on memory and CPU time. However, throughout this paper, we did not use such trivial boundary conditions. We restricted the boundary conditions either to the exact localized solution or the CW. A number of examples on localised solutions are considered in the following section, while the uniform, CW, solution of the NLSE, (1) considered here, is given by

$$\psi(x, t) = A_0 e^{i \left[\left(g_2 A_0^2 - \frac{k^2}{4g_1} \right) t + \frac{k}{2g_1} (x - x_0) \right]}, \quad (27)$$

from which we define

$$u(x, t) = A_0 \cos \left[\left(g_2 A_0^2 - \frac{k^2}{4g_1} \right) t + \frac{k}{2g_1} (x - x_0) \right], \quad (28)$$

$$v(x, t) = A_0 \sin \left[\left(g_2 A_0^2 - \frac{k^2}{4g_1} \right) t + \frac{k}{2g_1} (x - x_0) \right], \quad (29)$$

where A_0 , k , and x_0 being arbitrary real constants.

Finally, the method can be summarized with the following algorithm:

Algorithm:

- 1) *Initial profile, for $1 \leq i \leq n_x$: $a_0^i = u_0(x_i)$ and $b_0^i = v_0(x_i)$.*
- 2) *Boundary conditions, for $l > 0$, $1 \leq i \leq (p-1)/2$ and $n_x - (p-1)/2 < i \leq n_x$:*

$$a_l^i = \frac{1}{l!} \frac{\partial^l}{\partial t^l} u(x_i, t)|_{t=0},$$

$$b_l^i = \frac{1}{l!} \frac{\partial^l}{\partial t^l} v(x_i, t)|_{t=0},$$

[Eqs. (25) and (26)]

- 3) *Recursion relations, for $l > 0$, $(p-1)/2 < i \leq n_x - (p-1)/2$:*

$$a_l^i = a_l^i \left(a_0^i, b_0^i, \sum_{j=1}^{(p-1)/2} \bar{C}_j \left[b_{l-1}^{i+j} + b_{l-1}^{i-j} - 2b_{l-1}^i \right] \right),$$

$$b_l^i = b_l^i \left(a_0^i, b_0^i, \sum_{j=1}^{(p-1)/2} \bar{C}_j \left[a_{l-1}^{i+j} + a_{l-1}^{i-j} - 2a_{l-1}^i \right] \right).$$

[Eqs. (23), (24), and similar equations for the rest of coefficients.]

- 4) *Time evolution and update:*

$$a_0^i \leftarrow \sum_{l=0}^s a_l^i \Delta t^l, \tag{30}$$

$$b_0^i \leftarrow \sum_{l=0}^s b_l^i \Delta t^l. \tag{31}$$

- 5) *Return to step 3 with the updated values of a_0^i and b_0^i .*

The algorithm is also depicted schematically in Fig. 2.

III. ERROR ANALYSIS

The main aim here is to calculate and characterize the error of our method. As pointed out in the previous section, there are two main sources of error. The first source of error arises from the termination of the time power series at order s , namely $error_s$ given by Eq. (9). The second source of error is due to approximating the second derivative by the p -point formula, $error_p$ given by Eq. (22). We verify this understanding through the numerical solution of bright and dark solitons.

A. Bright soliton

The exact movable bright soliton solution of Eq. (1) can be expressed as

$$\psi(x, t) = A_0 \sqrt{\frac{2g_1}{g_2}} \operatorname{sech} \{A_0 [x - (x_0 + kt)]\} e^{i \left[\frac{k}{2g_1}(x-x_0) + \left(\frac{4A_0^2 g_1^2 - k^2}{4g_1} \right) (t-t_0) + \phi_0 \right]}, \quad (32)$$

where $g_1 g_2 > 0$, and the arbitrary real constants A_0 , x_0 , t_0 , k , and ϕ_0 physically define the height of the wave, spacial shift, temporal shift, soliton speed, and global phase, respectively.

The error is defined as

$$error = \max [|\psi_{\text{numerical}}(x_i, t_f)| - |\psi_{\text{exact}}(x_i, t_f)|], \quad 1 \leq i \leq n_x, \quad (33)$$

where t_f is the final time of evolution. In semi-log plots versus p for the 4 values of s , Fig. 3 shows the general behavior of a decreasing error that saturates at a certain value. Our analysis shows that the decreasing part corresponds to $error_p$ and the saturating part corresponds to $error_s$. For low values of p , the error in the p -point formula, $error_p$, is larger than the error in the order, $error_s$. With larger values of p , accuracy enhances such that $error_p$ becomes smaller than $error_s$, and thus the total error is dominated by $error_s$ which is independent of p . To verify this understanding, we calculate $error_p$, as given by Eq. (22) and plot it with the black filled circles where it is clear that the theoretical prediction of this part of error follows the numerical one. The order error, $error_s$, is calculated from Eq. (9), and is plotted with the dashed horizontal lines. Here again, the theoretical prediction for $error_s$ agrees very well with the numerical values. The figure shows clearly the interplay between the effects of s and p on the accuracy: Decreasing the error with p is limited by a saturation minimum set by s . We have repeated this calculation for decreasing time discretization but with keeping the final time the same. The purpose of this is to verify that the saturation values do indeed decrease according to Eq. (9), which is clearly the case as can be seen in all cases considered. It shows also, as expected, that decreasing Δt has the same effect as increasing the order. In Fig. 4, we show the effect of increasing the order on accuracy. The saturation levels correspond to $error_p$ where error is no longer depending on the order. For larger p , higher order is needed to reach saturation.

For realistic applications, it is important to keep the error small during long times of evolution. We show in Fig. 5 the time evolution of error up to $t = 40$ with different values of p . For $p = 3, 5, 7$, the error grows linearly with time for most of the time interval. For larger values of p , the error starts to saturate at a value that decreases with increasing p . For $p = 23$, the error saturates at the machine precision. Therefore, the numerical solution can be considered as exact up to the machine precision within the time interval considered. On a semi-logarithmic scale, we plot in Fig. 6 the error at the end of time evolution, $error(t = t_f)$, versus p , which shows how rapidly the error drops to the machine precision with increasing p . For longer time evolution, Fig. 7 shows that even with $p = 23$, the error starts to grow with time. Larger value of p is needed to get the error back to saturation.

Since using an exact analytical solution to calculate the boundary conditions is not the most general case, we investigate the effect of replacing the exact boundary conditions by approximate ones. For the bright soliton, all coefficients a_i^l and b_i^l at the boundaries, namely with $1 \leq i < (p-1)/2$ and $n_x - (p-1)/2 < i \leq n_x$, are set to zero. In Fig. 8, we show that using approximate boundary conditions leads to an error that is almost identical to that when exact boundary conditions are used.

B. Dark soliton

Solutions with finite background are typically more demanding computationally due to errors from the edges of the spacial domain. This introduces another source of error. In the present method, boundary points are fixed by boundary conditions through an exact or approximate analytical solutions while the bulk of the spacial grid is evolved according to the numerical method. The difference in evolution procedure generates high frequency oscillations stemming from the boundary between the points evolved with the numerical method and the points evolved with the boundary conditions.

The dark soliton we consider for comparison is given by

$$\psi(x, t) = A_0 \sqrt{\frac{-2g_1}{g_2}} \tanh\{A_0 [x - (x_0 + kt)]\} e^{-i[-\frac{k}{2g_1}(x-x_0) + \frac{8g_1^2 A_0^2 + k^2}{4g_1}(t-t_0) + \phi_0]}, \quad (34)$$

where $g_1 g_2 < 0$. Time evolution of error is shown in Fig. 9. Similar to the bright soliton case, the linear dependence of error on evolution time disappears with increasing p . However, it is noticed here that the saturation value for $p = 23$ is around 1.5×10^{-12} which is not at machine precision, as the case was with bright soliton. In Fig. 10, this can also be seen with error at the final evolution time plotted versus p . Investigating this behaviour further showed that it is due to the errors at the boundaries. Here, the background is finite and boundary errors appear more prominently unlike the case of zero background for bright soliton. A snapshot of the error is shown in Fig. 11 where it is clear that the error is significant only at the boundaries and the centre. The central error is associated with the structure of the dark soliton. The nature of the boundary error is different; it is caused, as mentioned above, by fixing the boundary points to fixed values and evolving the other points using the numerical scheme. For small p , the central error is dominant. Increasing p reduces both the central and boundary errors, but the boundary error saturates after a certain value of p , while the central error keeps decreasing. The boundary error becomes dominant for larger p . This is verified in Fig. 12 where we plot the central and boundary errors separately. While the central error is responsive to increasing p , where it ultimately decreases down to machine precision, the boundary error saturates at a larger value. Nonetheless, for the given parameters which are realistic, the total error is extremely small. We have verified that boundary errors can be reduced by increasing the order and size of spacial domain and then machine precision can be reached again. Investigating the effect of using approximate boundary conditions is shown in Fig. 13. Here we used the CW solution, (27), to calculate the boundary conditions (25) and (26) with the same parameters as used for the dark soliton in Fig. 9. Similar to the bright soliton case, the error using approximate boundary conditions is almost indistinguishable from that with exact boundary conditions.

IV. COMPARISON WITH OTHER METHODS

Among the many numerical methods developed to solve the NLSE, the so-called G-FDTD was shown to exceed by orders of magnitude the accuracy of all other methods [8–10, 26]. Therefore, we restrict the comparison to this method. We start by pointing out the similarities and differences between the G-FDTD and present method.

Both methods use a power series expansion to integrate the time operator. However, in the G-FDTD method, the Crank-Nicolson time stepping method is used and the expansion is restricted to odd powers of Δt . Here, we do not use the Crank-Nicolson time stepping and we include all powers in the time expansion, as shown in (5) and (6). The use of the Crank-Nicolson method reduces the error in the time evolution by one order of magnitude in Δt . This additional accuracy comes on

the expense of memory and run time cost; the evolution to $t + \Delta t$ requires the knowledge of the profiles at t and $t + \Delta t/2$ and this has to be done for the real and imaginary parts of the profile. Thus, it requires at least 4 times run time and memory size compared with typical time stepping. This additional memory and computing time cost will increase dramatically in higher dimensions. On the other hand, our analysis of the error in Fig. 3 has shown that, before the saturation region is reached, the error from the time evolution, $error_s$, is orders of magnitude smaller than the error from the spacial discretisation of the second derivative, $error_p$. Therefore, the additional accuracy brought by the use of the Crank-Nicolson time stepping is really not needed at this stage. It may have an advantage in case very long time evolution is needed, but even in that case, increasing the order, s , will lead to the required accuracy with less run time and memory storage.

In the G-FDTD method, an approximation was used in the calculation of the time evolution of the power expansion coefficients which is to consider the terms $|\psi(x, t)|$ as constants. This may not be justifiable with rapid and steep changes in $\psi(x, t)$. Here, we do not make this approximation. Our approach for the calculation of the coefficients of the power series is slightly different than that of Ref. [8–10, 26] allowing us to calculate the recursion relations and coefficients of the power series without any approximation.

Another point of similarity is that higher order discretisation of the second spacial derivative is used. In Ref. [8–10, 26], only the 3- and 5-point central difference point are used. Here, we use mostly up to the 23-point central difference formula to show that machine accuracy can indeed be reached with such a procedure. Our procedure allows for a straightforward and rather easy implementation of larger number of points.

The treatment of boundary conditions has also similarities and differences. Both methods use the exact localised initial solution or the CW solution to calculate the time evolution of the boundary points. In Ref. [9, 26], the first and last 6 points ($p = 5$ is used) were set to have the value of the exact solution for all times. In the present method, we set only the first and last 2 points to the exact values. The difference in number of boundary points is due to the difference in procedure of calculating the coefficients of the time power series. We believe it is more accurate to set only $(p - 1)/2$ boundary points and not $p + 1$, since the p -central difference formula correlates only the left or right $(p - 1)/2$ points to the central point. The effect of this difference in handling the boundary conditions will have an evident effect on solutions with finite background, such as dark and peregrine solitons, as we will point out below.

Bright soliton:

In the following, we consider the same parameters taken by Ref. [9, 26] to calculate the accuracy versus the exact solutions, namely $g_1 = -1$, $g_2 = -2$, $A_0 = 1$, $k = 4$, $x_0 = -10$. Since in Ref. [9, 26], the error is calculated as $error = \sqrt{(1/n_x) \sum_{i=1}^{n_x} (|\psi_{\text{numerical}}(x_i, t_f)| - |\psi_{\text{exact}}(x_i, t_f)|)^2}$, we use this definition in this and the dark soliton comparison. Table I shows that similar errors are obtained for $n_x = 100, 200, 300$, but not for $n_x = 400$ where our method gives about 40% smaller error. To understand this difference in error, we calculate the convergence rate defined by $R = \log(error_2/error_1)/\log(n_{x2}/n_{x1})$, where $error_{1,2} = error(n_{x1,2})$ calculated at two values of n_x . Convergence rate gives the exponent in the power law dependence of error on Δx , namely $error \propto (\Delta x)^R$. For the fourth order central point formula, used here, the error is proportional to $(\Delta x)^4$ and hence the convergence rate should be $R = 4$. Table I shows that indeed for both methods $R \approx 4$ for $n_x = 100, 200, 300$, but it is not so for the G-FDTD method with $n_x = 400$. To reach the theoretical convergence rate of 4, the value of Δt needs to be reduced which requires increasing n_t by the same factor so that the final time remains unchanged. This will of course require increased run time by the same factor. In Table II, we recalculate the error using $\Delta t = 10^{-6}$. Error and

convergence rate of the present method are almost the same as those with $\Delta t = 10^{-4}$, which is understood since the error at this stage is dominated by $error_p$. On the other hand, the error of the G-FDTD method at $n_x = 400$ has decreased and is now indeed close to that of the present method with a convergence rate approaching 4. The CPU time in this case is 170.7 s which is to be compared with 0.6 s for the present method at $n_x = 400$ in Table I. Thus, our code is more than 100 times faster than that of the G-FDTD method for about the same error and convergence rate. The difference in speed grows with larger n_x . Data for the G-FDTD code in Table I is not shown for $n_x > 400$, since it is unstable with $\Delta t = 10^{-4}$, while our code continues to be stable for much larger values of n_x with increasing accuracy and keeping the convergence rate approaching 4. With $\Delta t = 10^{-6}$, the G-FDTD code is stable for $n_x > 400$, but with convergence rate deviating from the theoretical value of 4 for larger n_x . Again, this can be fixed by decreasing Δt further which will require more run time. It should be noted that we do not use in the G-FDTD code the additional refinement, used in Ref. [26], of reducing the error to the machine precision from one step to the other, in order to preserve the norm and energy. This would significantly slower the G-FDTD code even further.

To show the high potential of the present method, we repeat the above calculations with larger number of central point formula. In Table III, we show the results for $p = 11, 15, 23$. The significant reduction in error is obvious with CPU times on the order of 1 s. The error can be seen to drop easily down to machine precision with $p = 23$ and $n_x > 350$. The convergence rates for $p = 11$ and $p = 15$ are close to the theoretical values of 10 and 14, respectively. However, for $p = 23$, the convergence rate reaches a maximum of 19.2 at $n_x = 400$ and then starts to drop. Unlike the similar case above with the G-FDTD method, it will not be possible to increase the convergence rate to the theoretical value of 22 by decreasing Δt since the error at this stage has reached the machine precision and does not any more depend on the parameters of the method. Remarkably, machine accuracy is reached with a CPU time less than 2 s.

A high accuracy method based on wavelets expansion, was developed in Ref. [17]. The present example compares with Example 2 in that reference. For $\Delta t = 0.01$ and $n_x = 200$, an error of 8.94×10^{-5} at $t = 1.0$ was obtained with a convergence rate close to 7. In the present method, this matches $s = 8$. Since we do not consider this value, we compare with $s = 7$ and $s = 9$, which have theoretical convergence rates 6 and 8, respectively. The error in these two cases turn out to be 1.05×10^{-4} and 1.16×10^{-5} , respectively. The CPU times are 0.01 s and 0.5 s for the former and latter cases, respectively. If we take the average of two error values for $s = 7$ and $s = 9$, the error value of the present method will be about 30% less than that of the Ref. [17]. Unfortunately, comparison of CPU time is not possible because they it is not reported in that reference.

Another important feature to present is the saturation of error at a constant minimum independent of Δt . This can be anticipated in view of our discussion of Fig. 3. Error will generally reduce with decreasing Δt , but when Δt is small enough, the error from time stepping will be less than that of the central point formula and thus the total error will be independent of Δt . The error in this case will be determined essentially by Eq. (22) but without the operator $\Delta t \partial/\partial t$ since the error at this stage is dominated by that of the central point formula

$$error_p = \max \left[\frac{(\Delta x)^{p-1}}{(p+1)!} \left| \frac{\partial |\psi^{p+1}(x, t)|}{\partial x^{p+1}} \right| \right]. \quad (35)$$

It is important to know the maximum Δt in this region for which the error is independent of Δt in order to save on the run time; no need to run the code with a very small, and hence time consuming Δt , while a larger value can produce the same error with less run time. In Fig. 14, this is manifested through a number of plots. At first, the upper panel shows that error of the present method reduces rather sharply to its saturation level, as predicted by (35), around $n_t \sim 465$ ($\Delta t = 1/n_t \approx 2.15 \times 10^{-3}$) over a range of $n_t = 2$. On the other hand, the error in

the G-FDTD method reduces in a slower rate to the same saturation level at around $n_t = 20000$ ($\Delta t = 1/n_t \approx 5 \times 10^{-5}$). The middle panel shows the huge difference in CPU times between the two methods. The bottom panel shows that while CPU time of the present method grows linearly with n_t , it grows quadratically with n_t for the G-FDTD method.

Dark soliton:

In Table IV, we show that the accuracy of the present method keeps increasing with increasing n_x while that of the G-FDTD saturates at a certain value. As explained above, the convergence rate is still far from the theoretical value of 4 and thus smaller Δt is needed in order to get smaller errors and better convergence rate.

V. OTHER EXAMPLES

Here we put the method under tests of cases involving high curvatures and fast time evolution, namely the Peregrine soliton and the two soliton molecule. The Peregrine soliton is characterised by high curvature at the time of its maximum peak. This will test the accuracy in the p -points formula for the second derivative. It will also test our treatment of the boundary conditions since the background for this soliton is finite. The two-soliton molecule is characterised by fast dynamics in the case when the two solitons coalesce. This will test the accuracy in the time power series method that integrates the time operator. Another important feature in both of these two solutions is that, unlike the previous two examples, their time evolution is nontrivial. In moving bright and dark solitons, the internal structure does not change. For the current examples, the internal structure changes with time, which will result in larger errors, as we will see below.

Peregrine soliton:

The exact Peregrine soliton of Eq. (1) takes the following expression

$$\psi(x, t) = \frac{1}{\sqrt{g_2}} \left[\frac{4 + i8(t - t_0)}{1 + 4(t - t_0)^2 + \frac{2}{g_1}(x - x_0)^2} - 1 \right] e^{i[t - t_0 + \phi_0]}, \quad (36)$$

where $g_2 > 0$. The initial profile is started at $t = -10$ and evolved till $t = 10$. Figure 15 shows the maximum error versus time for four values of p . The figure shows that the Peregrine soliton is highly demanding computationally, as hinted above. The error curves of $p = 23, 25, 27$ are almost the same. Increasing p will thus not enhance on the accuracy. Similar to the dark soliton, this terminal error is due to the finite background. It can be reduced by increasing the size of the spacial grid and increasing the order, s .

Two-bright soliton:

The two-bright soliton of Eq. (1) takes the form

$$\psi(x, t) = \frac{1}{\sqrt{g_2}} [\psi_1(x, t) + \psi_2(x, t)], \quad (37)$$

where

$$\psi_1(x, t) = \frac{M_{12} [\gamma_1^{-1}(x, t) + \gamma_2^*(x, t)] - M_{22} [\gamma_2^{-1}(x, t) + \gamma_2^*(x, t)]}{M_{12} M_{21} [\gamma_1^*(x, t) + \gamma_2^{-1}(x, t)] [\gamma_1^{-1}(x, t) + \gamma_2^*(x, t)] - M_{11} M_{22} [\gamma_1^{-1}(x, t) + \gamma_1^*(x, t)] [\gamma_2^{-1}(x, t) + \gamma_2^*(x, t)]},$$

$$\psi_2(x, t) = \frac{-M_{11} [\gamma_1^{-1}(x, t) + \gamma_1^*(x, t)] + M_{21} [\gamma_1^*(x, t) + \gamma_2^{-1}(x, t)]}{M_{12} M_{21} [\gamma_1^*(x, t) + \gamma_2^{-1}(x, t)] [\gamma_1^{-1}(x, t) + \gamma_2^*(x, t)] - M_{11} M_{22} [\gamma_1^{-1}(x, t) + \gamma_1^*(x, t)] [\gamma_2^{-1}(x, t) + \gamma_2^*(x, t)]},$$

$a_1 > 0$, $a_2 > 0$, $M_{jk} = 1/(\lambda_j + \lambda_k^*)$, $\gamma_j(x, t) = e^{\frac{\lambda_j}{\sqrt{2}g_1}(x-x_{0j}) + i[\lambda_j^2(t-t_0)/2 + \phi_{0j}]}$, $\lambda_j = \alpha_j + i\nu_j$, α_j , ν_j , x_{0j} , t_0 , and ϕ_{0j} are arbitrary real constants. Here, we compare our method with the split-step (SS) method and plot the numerical profiles of both methods together with the exact one in Fig. 16. While the profile of the present method is indistinguishable from the exact one, the profile of the SS method deviates significantly at large evolution times. It should be noted that we used $p = 3, 9, 23$ for our method. The $p = 3$ curve shows a slight deviation, but the $p = 9$ and $p = 23$, are almost identical to the exact profile. The error for these three values of p and the SS code are plotted in Fig. 17. Clearly, the $p = 9$ and $p = 23$ cases give extremely small errors for a long evolution time.

VI. INHOMOGENEOUS NLSE

Here, we present a generalisation of the method to the NLSE with an external potential. Then we consider an example of soliton scattering by a reflections potential well with a soliton speed close to the critical value for quantum reflection. The outcome, in this case reflection or transmission, is very sensitive to the accuracy of the numerical method used. The high accuracy provided by the present method is crucial for obtaining the correct scattering outcome and accounting accurately for the value of the critical speed.

In the presence of an external potential, $V(x)$, the NLSE can be expressed as

$$i \frac{\partial}{\partial t} \psi(x, t) + g_1 \frac{\partial^2}{\partial x^2} \psi(x, t) + g_2 |\psi(x, t)|^2 \psi(x, t) - V(x) \psi(x, t) = 0. \quad (38)$$

Writing the general solution in the cartesian complex form $\psi(x, t) = u(x, t) + i v(x, t)$, where $u(x, t)$ and $v(x, t)$ being real functions, and inserting in (38), generates two equations from the real and imaginary parts

$$g_2 u^3(x, t) + g_1 \frac{\partial^2}{\partial x^2} u(x, t) + g_2 u(x, t) v^2(x, t) - \frac{\partial}{\partial t} v(x, t) - V(x) u(x, t) = 0, \quad (39)$$

$$g_2 v^3(x, t) + g_1 \frac{\partial^2}{\partial x^2} v(x, t) + g_2 v(x, t) u^2(x, t) - \frac{\partial}{\partial t} u(x, t) - V(x) v(x, t) = 0. \quad (40)$$

Substituting the power series expansions (10) and (11), the recursion relations are obtained as

$$a_1 = -g_2 a_0^2 b_0 - g_2 b_0^3 + b_0 V(x) - g_1 b_0'', \quad (41)$$

$$a_2 = \frac{1}{2} [-2g_2 a_0 a_1 b_0 - g_2 a_0^2 b_1 - 3g_2 b_0^2 b_1 + b_1 V(x) - g_1 b_1''], \quad (42)$$

$$a_3 = \frac{1}{3} \left[-g_2 a_1^2 b_0 - 2g_2 a_0 a_2 b_0 - 2g_2 a_0 a_1 b_1 - 3g_2 b_0 b_1^2 - g_2 a_0^2 b_2 - 3g_2 b_0^2 b_2 + b_2 V(x) - g_1 b_2'' \right], \quad (43)$$

$$a_4 = \frac{1}{4} \left[-g_2 a_1^2 b_1 - g_2 b_1^3 - 2g_2 a_0 a_3 b_0 - 2g_2 a_0 a_2 b_1 - 6g_2 b_0 b_1 b_2 - 2g_2 a_1 a_2 b_0 - 2g_1 a_1 a_0 b_2 - g_2 a_0^2 b_3 - 3g_2 b_0^2 b_3 + b_3 V(x) - g_1 b_3'' \right], \quad (44)$$

$$b_1 = g_2 a_0 b_0^2 + g_2 a_0^3 - a_0 V(x) + g_1 a_0'', \quad (45)$$

$$b_2 = \frac{1}{2} [2g_2 a_0 b_0 b_1 + g_2 b_0^2 a_1 + 3g_2 a_0^2 a_1 - a_1 V(x) + g_1 a_1''], \quad (46)$$

$$b_3 = \frac{1}{3} \left[g_2 a_0 b_1^2 + 2 g_2 a_0 b_2 b_0 + 2 g_2 a_1 b_0 b_1 + 3 g_2 a_0 a_1^2 + g_2 a_2 b_0^2 + 3 g_2 a_0^2 a_2 - a_2 V(x) + g_1 a_2'' \right], \quad (47)$$

$$b_4 = \frac{1}{4} \left[g_2 a_1 b_1^2 + g_2 a_1^3 + 2 g_2 a_0 b_3 b_0 + 2 g_2 a_0 b_1 b_2 + 6 g_2 a_0 a_1 a_2 + 2 g_2 a_1 b_2 b_0 + 2 g_2 a_2 b_0 b_1 + g_2 b_0^2 a_3 + 3 g_2 a_0^2 a_3 - a_3 V(x) + g_1 a_3'' \right]. \quad (48)$$

The boundary conditions are treated here in a similar manner as in the homogeneous case, namely using Eqs. (25) and (26). Finally, the time evolution is determined by the algorithm of the previous section but using the above modified recursion relations.

Example: Soliton scattering by a reflectionless potential well

The bright soliton described by (32) is scattered by the following reflectionless potential well

$$V(x) = -\frac{V_0^2}{\cosh^2(\alpha x)}, \quad (49)$$

where V_0 and α being arbitrary real constants. It is established that below a critical speed, the soliton will reflect. This is known as quantum reflection since it occurs due to a repulsive force of interaction between a trapped mode formed from the tail of the incoming soliton with the rest of the soliton. We use a soliton speed very close to the critical value and observe the outcome in terms of accuracy of the method. We also compare our results with the SS method. In Fig. 18, we plot the soliton profiles long after scattering by the potential. For the crudest version of our code, namely $p = 3$ and $n_x = 512$, the soliton transmits. Using the same parameters, the SS code leads to reflection. Since an exact analytical solution is not available, we use the comparative analysis to have an estimate on the accuracy of our results. We increase n_x till the profile saturates at a certain shape. Considering four values of n_x , Fig. 19 shows that the profile of our code is saturating in the transmission region at around $x = 35$. The profile of the SS code transfers from reflection to the transmission region and gradually approaches the profile of the present method. This is shown more clearly where we use $p = 23$ to see that saturation is already reached where the shape and position of the profiles are the same. There are small deviations for the $n_x = 512$ case but they gradually disappear with increasing n_x .

VII. TWO-COUPLED NLSE

Here we apply the method to two-coupled NLSE and use the dark-bright soliton exact solution to check the accuracy. The two-coupled NLSE reads

$$i \frac{\partial}{\partial t} \psi_1(x, t) + g_{10} \frac{\partial^2}{\partial x^2} \psi_1(x, t) + [g_{11} |\psi_1(x, t)|^2 + g_{12} |\psi_2(x, t)|^2] \psi_1(x, t) = 0, \quad (50)$$

$$i \frac{\partial}{\partial t} \psi_2(x, t) + g_{20} \frac{\partial^2}{\partial x^2} \psi_2(x, t) + [g_{21} |\psi_1(x, t)|^2 + g_{22} |\psi_2(x, t)|^2] \psi_2(x, t) = 0, \quad (51)$$

where, $\psi_1(x, t)$ and $\psi_2(x, t)$ are complex functions, and g_{10} , g_{20} , g_{11} , g_{12} , g_{21} and g_{22} are real constants. The two components of the general solution are written in the cartesian complex form

$$\psi_1(x, t) = u_1(x, t) + i v_1(x, t), \quad (52)$$

$$\psi_2(x, t) = u_2(x, t) + i v_2(x, t), \quad (53)$$

where $u_1(x, t)$, $v_1(x, t)$, $u_2(x, t)$, and $v_2(x, t)$ being real functions. Inserting in (50) and (51), generates the following four equations from the real and imaginary parts

$$g_{11} u_1^3(x, t) + g_{12} u_1(x, t) u_2^2(x, t) + g_{11} u_1(x, t) v_1^2(x, t) + g_{12} u_1(x, t) v_2^2(x, t) - \frac{\partial}{\partial t} v_1(x, t) + g_{10} \frac{\partial^2}{\partial x^2} u_1(x, t) = 0, \quad (54)$$

$$g_{11} u_1^2(x, t) v_1(x, t) + g_{12} u_2^2(x, t) v_1(x, t) + g_{11} v_1^3(x, t) + g_{12} v_1(x, t) v_2^2(x, t) + \frac{\partial}{\partial t} u_1(x, t) + g_{10} \frac{\partial^2}{\partial x^2} v_1(x, t) = 0, \quad (55)$$

$$g_{22} u_2^3(x, t) + g_{21} u_1^2(x, t) u_2(x, t) + g_{21} u_2(x, t) v_1^2(x, t) + g_{22} u_2(x, t) v_2^2(x, t) - \frac{\partial}{\partial t} v_2(x, t) + g_{20} \frac{\partial^2}{\partial x^2} u_2(x, t) = 0, \quad (56)$$

$$g_{21} u_1^2(x, t) v_2(x, t) + g_{22} u_2^2(x, t) v_2(x, t) + g_{22} v_2^3(x, t) + g_{21} v_1^2(x, t) v_2(x, t) + \frac{\partial}{\partial t} u_2(x, t) + g_{20} \frac{\partial^2}{\partial x^2} v_2(x, t) = 0. \quad (57)$$

Then we expand $u_1(x, t)$, $v_1(x, t)$, $u_2(x, t)$, and $v_2(x, t)$ in the following power series

$$u_1(x, t) = \sum_{l=0}^s a_l(x) \Delta t^l, \quad (58)$$

$$v_1(x, t) = \sum_{l=0}^s b_l(x) \Delta t^l, \quad (59)$$

$$u_2(x, t) = \sum_{l=0}^s c_l(x) \Delta t^l, \quad (60)$$

$$v_2(x, t) = \sum_{l=0}^s d_l(x) \Delta t^l, \quad (61)$$

where the function coefficients are defined by

$$a_l(x) = \frac{1}{l!} \frac{\partial^l}{\partial t^l} u_1(x, t)|_{t=0}, \quad (62)$$

$$b_l(x) = \frac{1}{l!} \frac{\partial^l}{\partial t^l} v_1(x, t)|_{t=0}, \quad (63)$$

$$c_l(x) = \frac{1}{l!} \frac{\partial^l}{\partial t^l} u_2(x, t)|_{t=0}, \quad (64)$$

$$d_l(x) = \frac{1}{l!} \frac{\partial^l}{\partial t^l} v_2(x, t)|_{t=0}. \quad (65)$$

Substituting these series expansions in Eqs. (54)-(57), recursion relations for the coefficient functions $a_l(x)$, $b_l(x)$, $c_l(x)$, and $d_l(x)$ are derived and listed in Appendix B for convenience, as they turn out to be lengthy. The boundary points with $1 \leq i \leq (p-1)/2$ and $n_x - (p-1)/2 < i \leq n_x$, are set to the values

$$a_l^i = \frac{1}{l!} \frac{\partial^l}{\partial t^l} u_1(x_i, t)|_{t=0}, \quad (66)$$

$$b_l^i = \frac{1}{l!} \frac{\partial^l}{\partial t^l} v_1(x_i, t)|_{t=0}, \quad (67)$$

$$c_l^i = \frac{1}{l!} \frac{\partial^l}{\partial t^l} u_2(x_i, t)|_{t=0}, \quad (68)$$

$$d_i^i = \frac{1}{i!} \frac{\partial^i}{\partial t^i} v_2(x_i, t)|_{t=0}. \quad (69)$$

The algorithm described in Section II is then applied to calculate the evolution of the profiles $u_1(x, t)$, $v_1(x, t)$, $u_2(x, t)$, and $v_2(x, t)$.

Example: Dark-bright soliton

The exact dark-bright soliton solution of the two-coupled NLSE, Eqs. (50) and (51), is given by

$$\psi_1(x, t) = A_0 \sqrt{\frac{g_{12} g_{20} - g_{10} g_{22}}{g_{11} g_{20} - g_{10} g_{21}}} \tanh \left\{ A_0 \sqrt{\frac{g_{12} g_{21} - g_{11} g_{22}}{2(g_{10} g_{21} - g_{11} g_{20})}} [(x - x_0) - k(t - t_0)] \right\} \times e^{i \left\{ (t-t_0) \left[\frac{g_{11} A_0^2 (g_{12} g_{20} - g_{10} g_{22})}{g_{11} g_{20} - g_{10} g_{21}} - \frac{k^2}{4 g_{10}} \right] + \frac{k(x-x_0)}{2 g_{10}} \right\}}, \quad (70)$$

$$\psi_2(x, t) = A_0 \operatorname{sech} \left\{ A_0 \sqrt{\frac{g_{12} g_{21} - g_{11} g_{22}}{2(g_{10} g_{21} - g_{11} g_{20})}} [(x - x_0) - k(t - t_0)] \right\} \quad (71)$$

$$\times e^{\frac{i \{ 2g_{12}g_{20}g_{21}A_0^2(t-t_0) + 2g_{11}g_{20}g_{20}g_{22}A_0^2(t-t_0) + kg_{11}g_{20}[2(x-x_0) - k(t-t_0)] + 4g_{10}g_{21}g_{20}g_{22}A_0^2(t-t_0) + kg_{10}g_{21}[2(x-x_0) + k(t-t_0)] \}}{4g_{20}(g_{11}g_{20} - g_{10}g_{21})}}, \quad (72)$$

where A_0 , k , x_0 , and t_0 are arbitrary real constants and all quantities under the square root must be positive.

In Fig. 20, we plot the error versus x in the numerical solution of both components, $\psi_1(x, t)$ and $\psi_2(x, t)$, at $t = 40$ and using $p = 23$ and $s = 4$. Clearly, the error in both components is extremely small even for such a long evolution time.

VIII. CONCLUSIONS AND OUTLOOK

We have presented a high accuracy numerical method that solves the initial value problem of the fundamental, inhomogeneous, and coupled NLSE. The method employed an iterative power series for time stepping and a multi-point formula for the spacial discretisation of the second derivative. The method is characterised by a systematic increase in accuracy in terms of the two parameters s and p , representing the maximum power of the time power series and number of points in the multi-point formula, respectively. As a result, the accuracy was shown via some examples to reach the machine precision in a rather short computing time.

Detailed analysis of the different sources of error was performed. Errors arising from the time power series, $error_s$, and the multi-point formula, $error_p$, were characterised and accounted theoretically. Error from the boundaries, which is more significant for solutions with uniform background, was shown to reduce with higher order of the time power series and larger system size.

We compared the present method with two other methods representing the finite difference and spectral methods. For finite difference methods, the G-FDTD method was selected for comparison due to its high accuracy and similarity to our method. For the spectral methods, we compared our results with the Fourier split-step method. We have pointed out the similarities and differences between our method and the G-FDTD method and shown that the present method is characterised by a faster computing time and higher convergence rate. The accuracy and computing time exceed by far those of the split-step method. The method is extended to the inhomogeneous NLSE and applied to the scattering of a bright soliton by a reflectionless potential. This example showed the importance of high accuracy to capture the correct scattering outcome near the critical value of soliton speed separating quantum reflection from transmission. We have also generalised the method to the two-coupled NLSE and considered the example of dark-bright soliton.

It is straightforward to extend the method to higher dimensions. The method can also be extended to NLSE with higher order terms such as third dispersion and Raman scattering, etc. It should be noted however, that the method does not apply to time-dependent potentials and time-dependent coefficients. In obtaining the recursion relations of the time power series, this was implicitly assumed. Extending the method to evolution equations with higher time derivatives is also possible, but with a different recursive structure.

In conclusion, we believe the method presented here will be very useful for realistic efficient numerical solutions of nonlinear evolution equations.

Acknowledgment

The authors acknowledge the support of UAE University through grants UAEU-UPAR (1) 2019 and UAEU-UPAR (11) 2019.

Tables

$\Delta t = 1 \times 10^{-4}$			
Present method			
n_x	error	CPU time(s)	convergence rate
100	2.04764×10^{-2}	0.193	
200	1.24616×10^{-3}	0.332	4.06753
300	2.49757×10^{-4}	0.465	3.98046
400	7.95110×10^{-5}	0.595	3.9902
500	3.26624×10^{-5}	1.030	3.99593
600	1.57757×10^{-5}	0.990	3.99889
700	8.5228×10^{-6}	1.072	4.00048
800	4.9986×10^{-6}	1.186	4.00136
900	3.1216×10^{-6}	1.463	4.00185
1000	2.0486×10^{-6}	1.707	4.00212
G – FDTD			
n_x	error	CPU time(s)	convergence rate
100	2.11658×10^{-2}	0.415	
200	1.25608×10^{-3}	0.796	4.07473
300	2.68115×10^{-4}	1.195	3.80880
400	1.43054×10^{-4}	1.572	2.18364

TABLE I: Error data for bright soliton given by (32) with $g_1 = -1$, $g_2 = -2$, $A_0 = 1$, $k = 4$, $x_0 = -10$, $p = 5$, $s = 3$. The G-FDTD code diverges for $n_x > 400$.

$\Delta t = 1 \times 10^{-6}$			
Present method			
n_x	error	CPU time(s)	convergence rate
100	2.04764×10^{-2}	1.600×10^1	
200	1.24616×10^{-3}	3.387×10^1	4.06753
300	2.49757×10^{-4}	4.998×10^1	3.98046
400	7.95110×10^{-5}	6.462×10^1	3.9902
500	3.26623×10^{-5}	9.762×10^1	3.99593
600	1.57757×10^{-5}	1.015×10^2	3.99889
700	8.5228×10^{-6}	1.167×10^2	4.00048
800	4.9986×10^{-6}	1.321×10^2	4.00136
900	3.1216×10^{-6}	1.491×10^2	4.00185
1000	2.0485×10^{-6}	1.833×10^2	4.00213
G – FDTD			
n_x	error	CPU time(s)	convergence rate
100	2.11482×10^{-2}	4.066×10^1	
200	1.26552×10^{-3}	8.348×10^1	4.06273
300	2.52158×10^{-4}	1.274×10^2	3.9786
400	7.99569×10^{-5}	1.707×10^2	3.99249
500	3.27135×10^{-5}	2.095×10^2	4.00504
600	1.57349×10^{-5}	2.518×10^2	4.01439
700	8.4839×10^{-6}	2.901×10^2	4.00714
800	5.0105×10^{-6}	3.305×10^2	3.94393
900	3.2231×10^{-6}	3.769×10^2	3.7457
1000	2.2738×10^{-6}	4.246×10^2	3.31165

TABLE II: Error data for bright soliton given by (32) with $g_1 = -1$, $g_2 = -2$, $A_0 = 1$, $k = 4$, $x_0 = -10$, $p = 5$, $s = 3$.

$p = 11$			
n_x	error	CPU time (s)	convergence rate
50	7.41644×10^{-2}	0.246	
100	8.4102×10^{-4}	0.384	6.55562
150	2.38048×10^{-5}	0.544	8.86396
200	1.67858×10^{-6}	0.679	9.27171
250	2.0163×10^{-7}	0.777	9.53988
300	3.46857×10^{-8}	0.888	9.68916
350	7.7177×10^{-9}	0.925	9.77911
400	2.0819×10^{-9}	1.009	9.83856
450	6.517×10^{-10}	1.136	9.88372
500	2.296×10^{-10}	1.319	9.92345
$p = 15$			
50	6.14867×10^{-2}	0.381	
100	2.5016×10^{-4}	0.428	8.05579
150	2.63863×10^{-6}	0.711	11.3185
200	8.60224×10^{-8}	0.754	11.9689
250	5.29238×10^{-9}	0.946	12.5517
300	5.04834×10^{-10}	1.069	12.9353
350	6.64545×10^{-11}	1.138	13.1947
400	1.11947×10^{-11}	1.321	13.3739
450	2.29149×10^{-12}	1.474	13.4992
500	5.48892×10^{-13}	1.747	13.5921
$p = 23$			
50	4.89514×10^{-2}	0.517	
100	8.71723×10^{-5}	0.695	9.26496
150	3.00017×10^{-7}	0.894	14.1034
200	4.07153×10^{-9}	0.950	15.0330
250	1.02235×10^{-10}	1.160	16.5858
300	4.04200×10^{-12}	1.204	17.7837
350	2.30026×10^{-13}	1.459	18.6516
400	1.77624×10^{-14}	1.737	19.2312
450	3.50575×10^{-15}	2.046	13.8093
500	2.67075×10^{-15}	2.280	2.58748

TABLE III: Error data of the present method for bright soliton given by (32) with $g_1 = -1$, $g_2 = -2$, $A_0 = 1$, $k = 4$, $x_0 = -10$, $\Delta t = 10^{-4}$, $s = 4$.

Present method			
n_x	error	CPU time (s)	convergence rate
100	7.00299×10^{-3}	$3. \times 10^{-2}$	
200	3.01673×10^{-4}	3.6×10^{-2}	4.56963
300	6.11528×10^{-5}	5.7×10^{-2}	3.95232
400	1.96238×10^{-5}	$7. \times 10^{-2}$	3.96245
500	8.0955×10^{-6}	1.07×10^{-1}	3.97687
600	3.9212×10^{-6}	1.07×10^{-1}	3.98333
700	2.1266×10^{-6}	1.4×10^{-1}	3.97537
800	1.2586×10^{-6}	1.25×10^{-1}	3.93352
900	8.032×10^{-7}	1.4×10^{-1}	3.81766
1000	5.518×10^{-7}	1.77×10^{-1}	3.56716
G – FDTD			
100	7.37839×10^{-3}	2.3×10^{-2}	
200	4.71382×10^{-4}	3.8×10^{-2}	3.96834
300	2.4642×10^{-4}	5.6×10^{-2}	1.59972
400	2.11859×10^{-4}	6.6×10^{-2}	5.2529×10^{-1}
500	2.02573×10^{-4}	8.0×10^{-2}	2.0086×10^{-1}
600	1.99137×10^{-4}	1.13×10^{-1}	9.385×10^{-2}
700	1.97577×10^{-4}	1.11×10^{-1}	5.100×10^{-2}
800	1.9676×10^{-4}	1.25×10^{-1}	3.105×10^{-2}
900	1.96282×10^{-4}	1.5×10^{-1}	2.063×10^{-2}
1000	1.95979×10^{-4}	1.6×10^{-1}	1.469×10^{-2}

TABLE IV: Error data for dark soliton given by (34) with $g_1 = 1/2$, $g_2 = -4$, $A_0 = 1$, $k = 4$, $x_0 = -10$, $p = 5$, $s = 3$. Note that in Ref. [9], the function given by (24) is not a dark soliton solution to Eq. (1) (also Eq. (1) in Ref. [9]) with the given values of $g_1 = 1$ and $g_2 = -4$. Instead, $g_1 = 1/2$, $g_2 = -4$ are the correct ones.

Figures

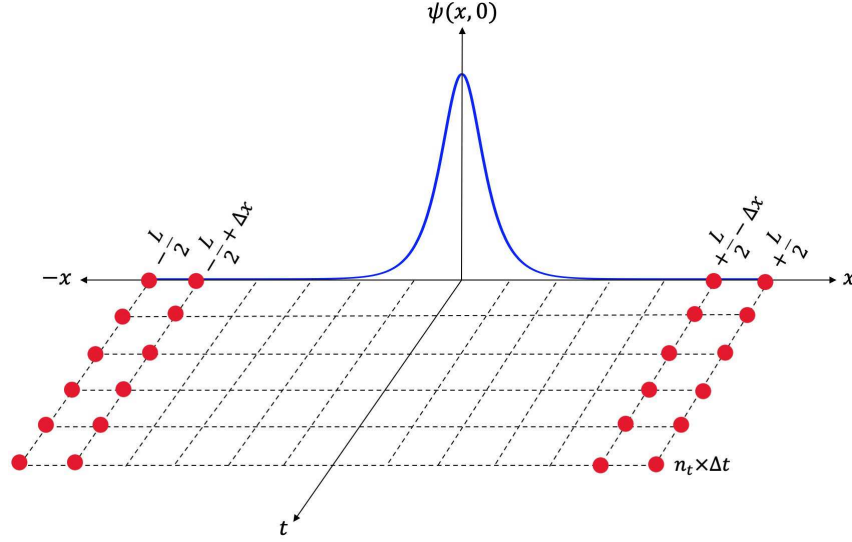


FIG. 1: Schematic diagram showing the initial profile (blue curve) and boundary points (red dots) for the case with $p = 5$. Number of the boundary points in each side of the grid equals $(p - 1)/2$. Each point is a part of a sequence of n_t points along the t -axis.

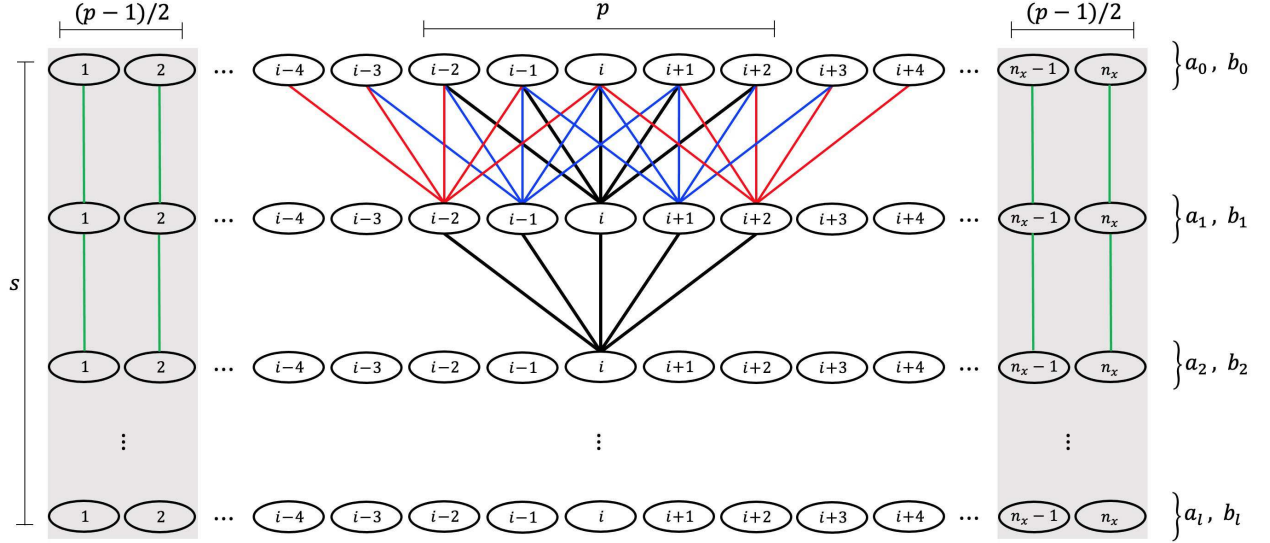


FIG. 2: Schematic figure depicting the algorithm of the present method. The figure is based on the special case of $p = 5$. Each coefficient, a_l or b_l , is calculated from 5 points of the previous order, a_{l-1} and b_{l-1} , according to Eqs. (23) and (24), and similar equations for the rest of coefficients. The first and last two points are calculated by the boundary conditions according to Eqs. (25) and (26).

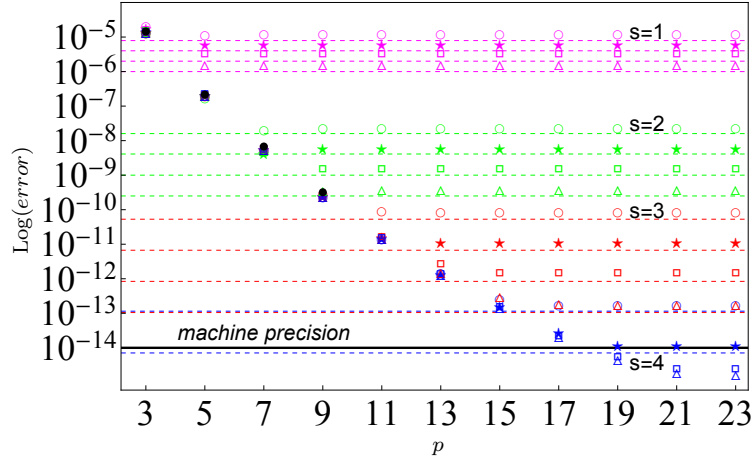


FIG. 3: Error in the numerical solution of Eq. (1) using the bright soliton (32) as an initial profile for different values of p , s , and Δt . Black filled circles correspond to $error_p$, as predicted by (22) for $p = 3, 5, 7, 9$. Horizontal dashed lines correspond to $error_s$, as predicted by Eq. (9). The thick line near the bottom indicates the machine precision, 10^{-14} . For each order the calculation is performed with Δt (circles), $\Delta t/2$ (stars), $\Delta t/4$ (squares), and $\Delta t/8$ (triangles). Parameters: $\Delta t = 0.001$, $n_x = 500$, $L = 40$, $\Delta x = L/(n_x - 1)$, $k = 4.0$, $x_0 = 0.0$, $A_0 = 1.0$, $g_1 = -1$, $g_2 = -2$, and for all points $t_f = n_t \times \Delta t = 1$.

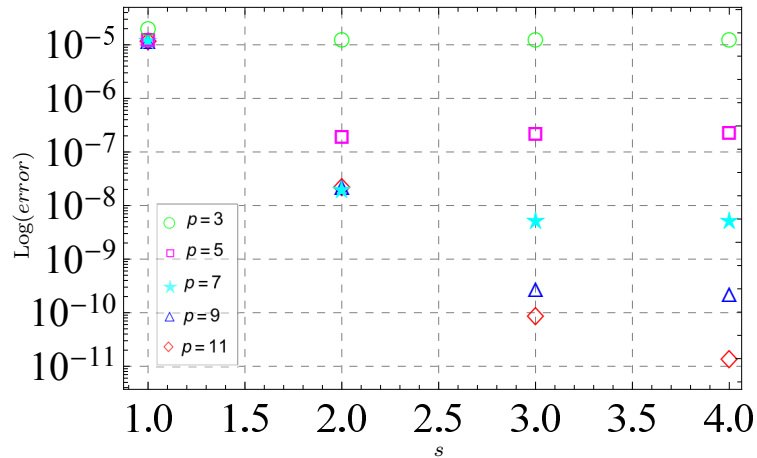


FIG. 4: Error in the numerical solution of the bright soliton corresponding to Eq. (32) versus s and different values of p in semi-log scale. Parameters: $\Delta t = 0.001$, $n_x = 500$, $n_t = 1$, $L = 40$, $\Delta x = L/(n_x - 1)$, $k = 4.0$, $x_0 = 0.0$, $A_0 = 1.0$, $g_1 = -1$, $g_2 = -2$. The circles, squares, stars, triangles, and diamonds indicate the maximum error with $p = 3, 5, 7, 9, 11$, respectively. For $p = 13, 15, 17, 19, 21, 23$, the points, which are not shown here, overlap with the diamonds ($p = 11$).

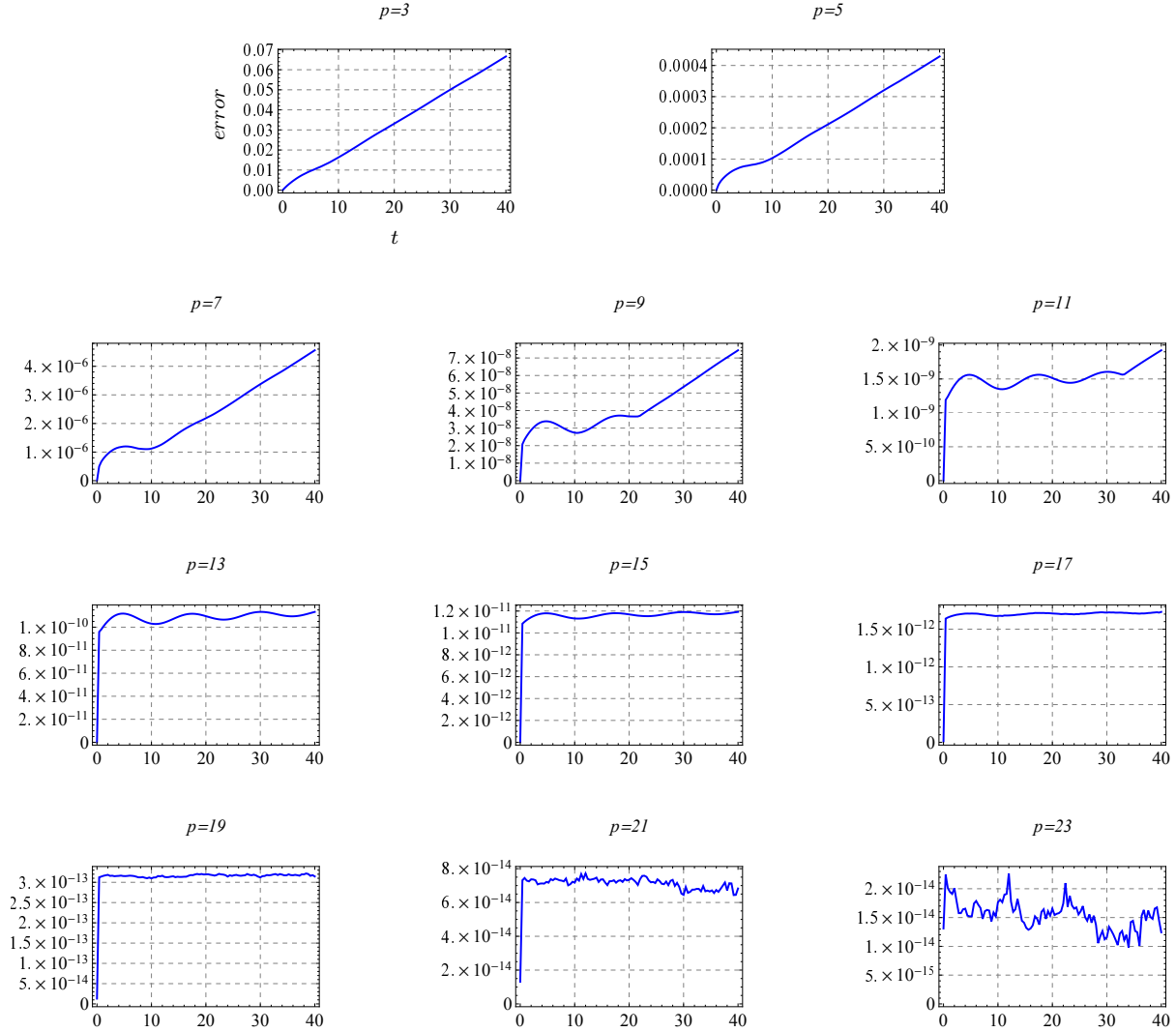


FIG. 5: Error evolution in the numerical solution of the bright soliton corresponding to (32). Fourth order power series expansion is used for all cases. For $p \geq 13$, the error saturates to a value independent of time. Machine precision is reached with $p = 23$. Parameters: $n_x = 8000$, $n_t = 80000$, $L = 800$, $\Delta t = 0.0005$, $\Delta x = L/(n_x - 1)$, $k = 1.0$, $x_0 = 0.0$, $A_0 = 1.0$, $g_1 = 1/2$, $g_2 = 1$.

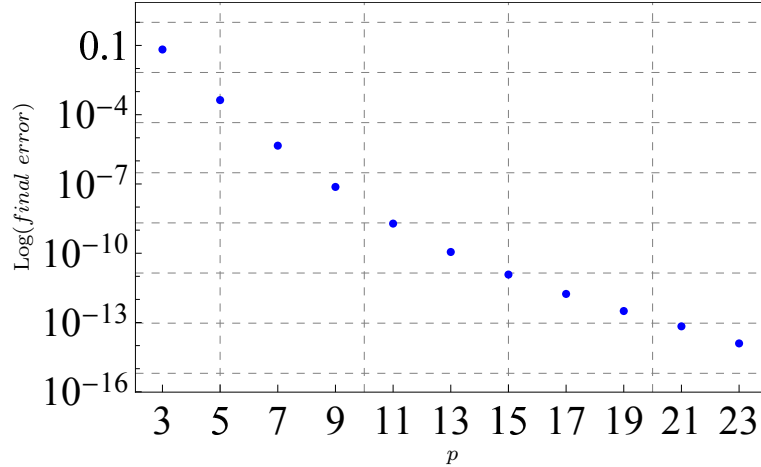


FIG. 6: Error at the final evolution time for sub-figures of Fig. 5 on a semi-log scale. For small values of p , the points approach the asymptote $\text{Log}(\text{final error}) = 17.60 - 15.78 \text{Log}(p)$, which gives: $\text{final error} = 4.40 \times 10^7 p^{-15.8}$.

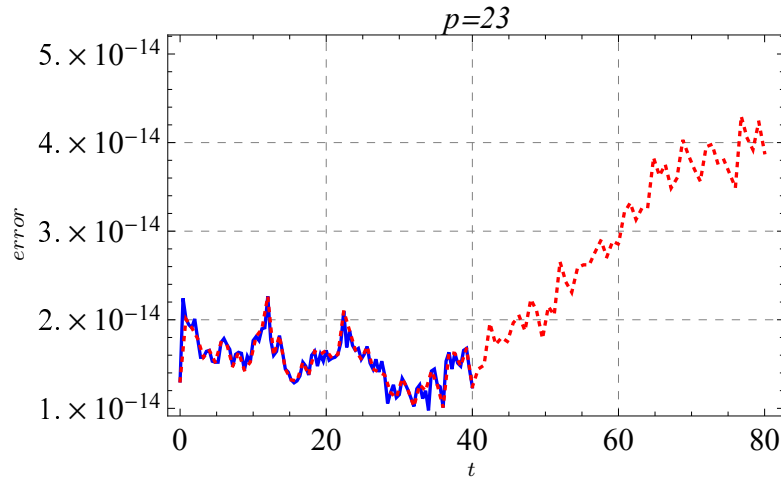


FIG. 7: Error evolution in the numerical solution of the bright soliton corresponding to Eq.(32). Dotted red curve corresponds to $p = 23$ of Fig. 5 with double evolution time. Fourth order power series expansion is used in this case. The corresponding curve from Fig. 5 is re-plotted here, with solid blue, and can be distinguished in the time interval $[0, 40]$. Parameters: $n_x = 8000$, $n_t = 160000$, $L = 800$, $\Delta t = 0.0005$, $\Delta x = L/(n_x - 1)$, $k = 1.0$, $x_0 = 0.0$, $A_0 = 1.0$, $g_1 = 1/2$, $g_2 = 1$.

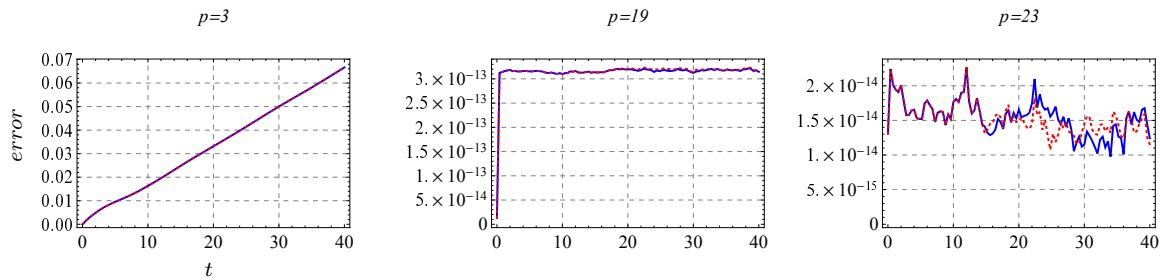


FIG. 8: Error evolution in the numerical solution of the bright soliton corresponding to Eq. (32). Dotted red curve corresponds to approximate boundary conditions. Solid blue curve corresponds to exact boundary conditions. Fourth order power series expansion is used for all cases. Parameters used are the same of those in Fig. 5.

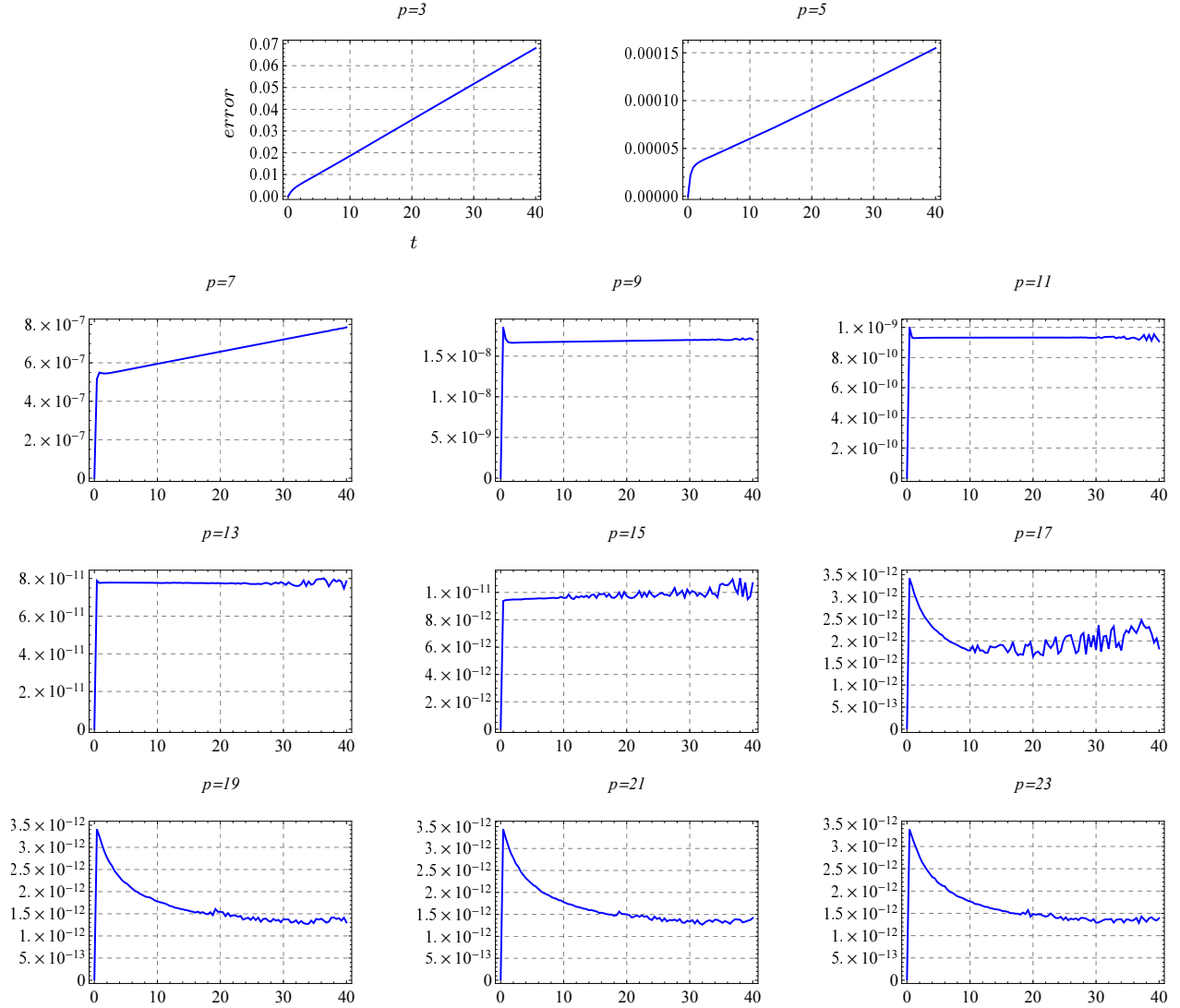


FIG. 9: Error evolution in the numerical solution of the dark soliton corresponding to Eq.(34) using increasing number of points in the second derivative discretization. Fourth order power series expansion is used for all cases. For $p > 7$, the error saturates at a value independent of t . The saturation value decreases with p . Parameters: $n_x = 4000$, $n_t = 80000$, $L = 400$, $\Delta t = 0.0005$, $\Delta x = L/(n_x - 1)$, $k = 1.0$, $x_0 = 0.0$, $A_0 = 1.0$, $g_1 = 1/2$, $g_2 = -1$.

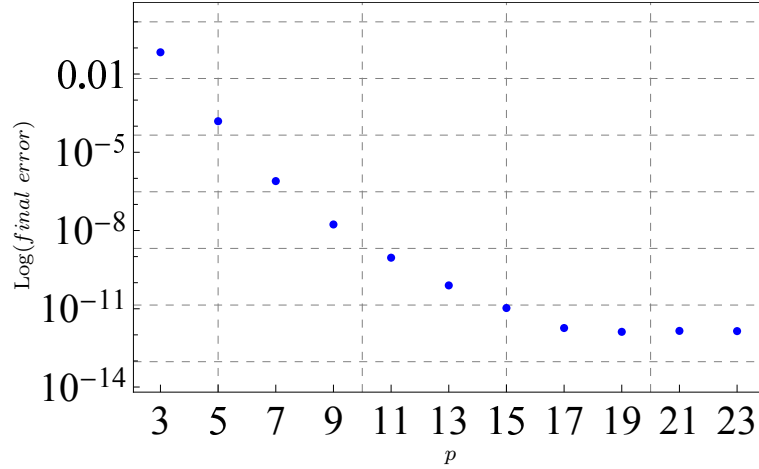


FIG. 10: Error at the final evolution time for sub-figures of Fig. 9 on a semi-log scale. For small values of p , the points approach the asymptote $\text{Log}(\text{final error}) = -6.22972 - 6.97164 \text{Log}(p)$, leading to $\text{final error} = 0.00197 p^{-6.9716}$.

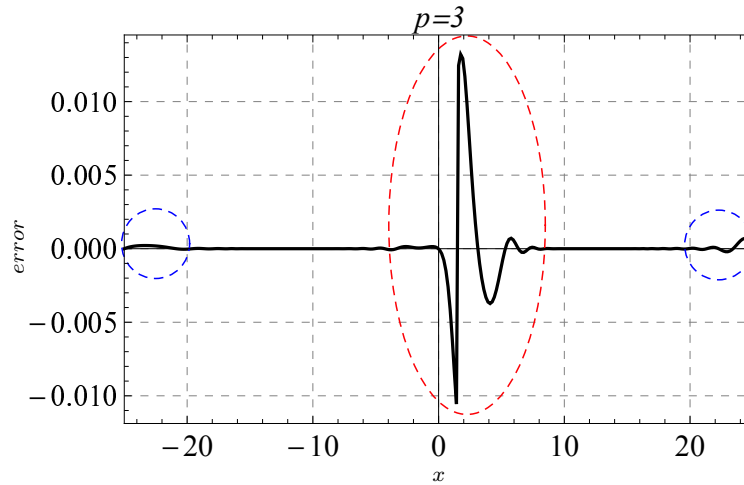


FIG. 11: Snapshot of error in the numerical solution of the dark soliton given by Eq. (34) at $t = 1.5$. The circles in dashed blue show the source of error from the edges and the circle in dashed red shows the source of error from the center. Parameters: $p = 3$, $s = 4$, $n_x = 300$, $n_t = 1000$, $L = 50$, $\Delta t = 0.01$, $\Delta x = L/(n_x - 1)$, $k = 1.0$, $x_0 = 0.0$, $A_0 = 1.0$, $g_1 = 1/2$, $g_2 = -1$.

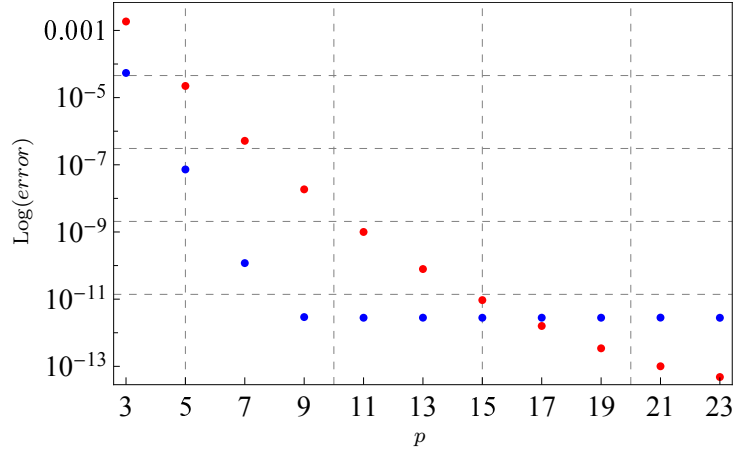


FIG. 12: Error at the edge and center of the spatial grid plotted in a semi-log scale. Red and blue points correspond to error at the centre and edges of the spacial grid, respectively. Each point corresponds to the error in a subfigure of Fig. 9 for the same value of p and $t = 40$. Parameters used are the same of those in Fig. 9.

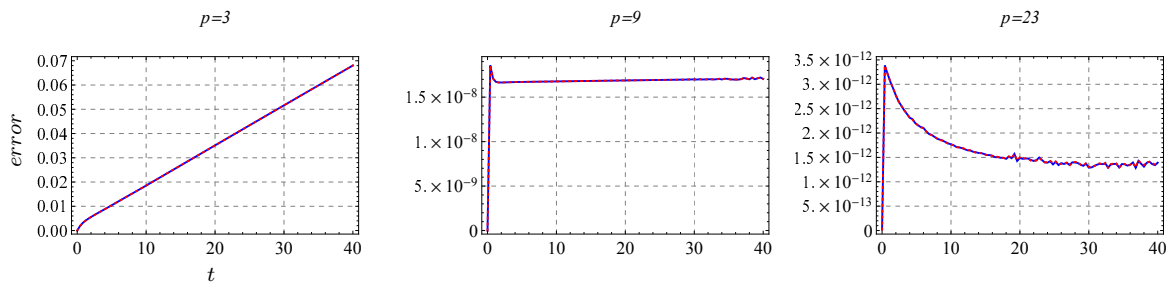


FIG. 13: Error evolution in the numerical solution of the dark soliton given by Eq.(34). The dotted red curve corresponds to approximate boundary conditions. The solid blue curve corresponds to exact boundary conditions. Fourth order power series expansion is used for all cases. Parameters used are the same of those in Fig. 9.

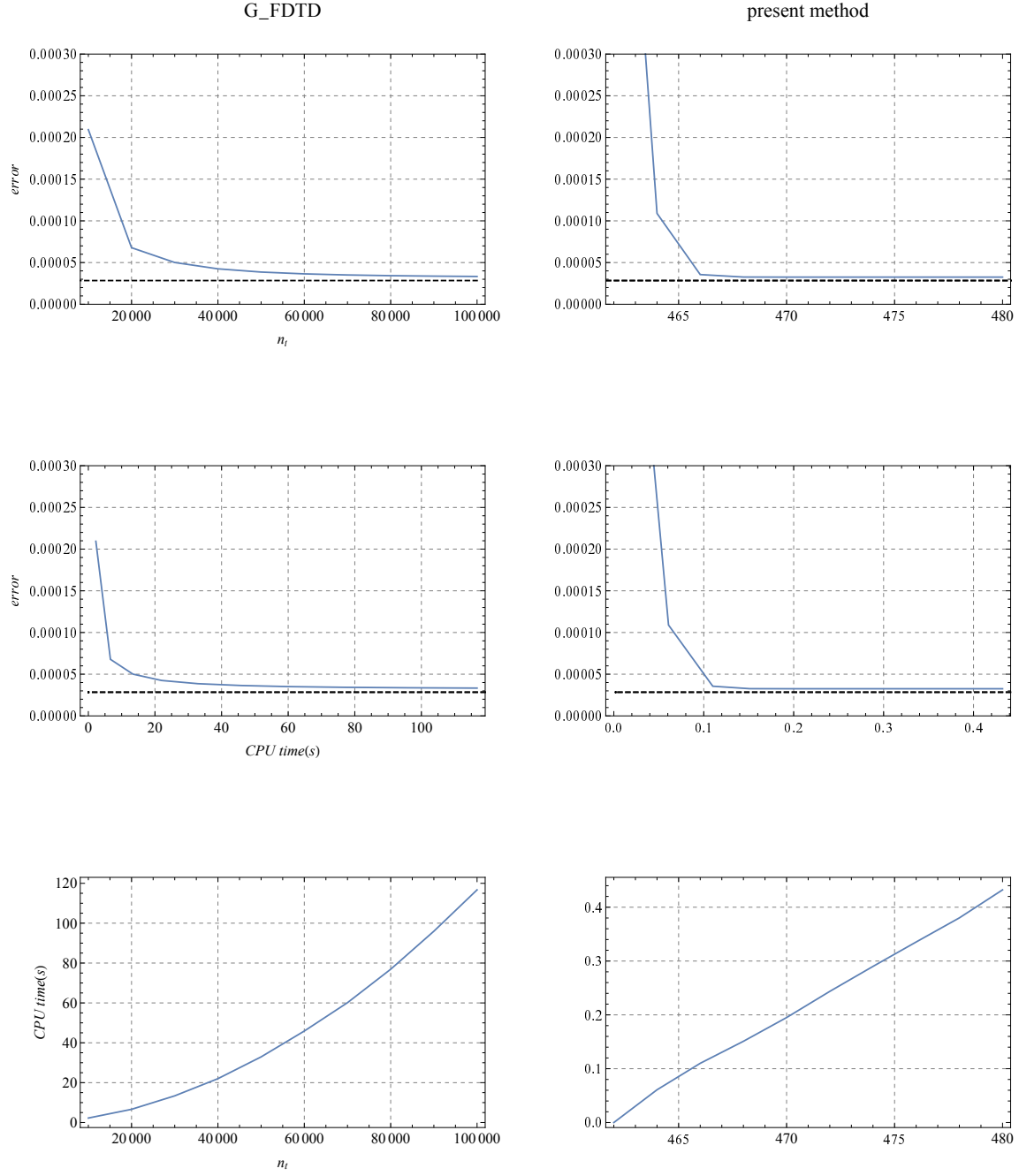


FIG. 14: Error and CPU time of the numerical bright soliton solution obtained by the present and G-FDTD methods. Error is calculated using the exact analytical bright soliton solution (32). Horizontal dashed asymptote corresponds the theoretical estimate given by (35). Parameters: $g_1 = -1$, $g_2 = -2$, $A_0 = 1$, $t, x_0 = -10$, $p = 5$, $s = 3$, $n_x = 500$.

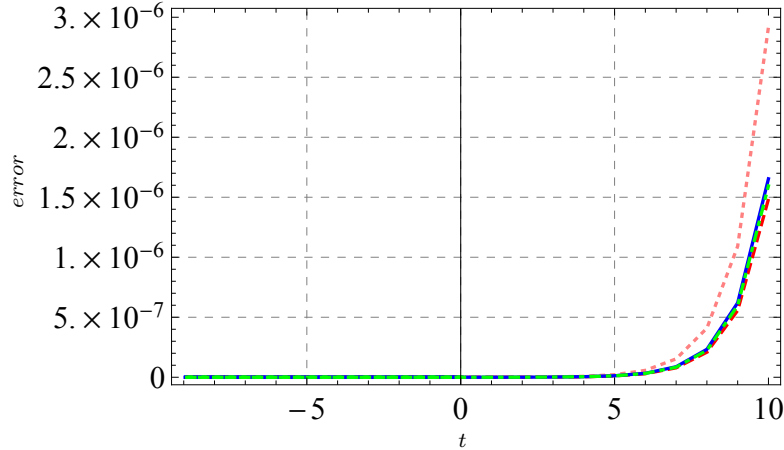


FIG. 15: Error evolution in the numerical solution of the Peregrine soliton given by Eq. (36) using increasing number of points in the second derivative discretization. Dotted pink curve corresponds to $p = 9$, dashed red curve corresponds to $p = 23$, solid black curve corresponds to $p = 25$, and green dotted-dashed green curve corresponds to $p = 27$. Fourth order power series expansion is used for all cases. Parameters: $n_x = 2000$, $n_t = 200000$, $L = 50$, $\Delta t = 0.0001$, $\Delta x = L/(n_x - 1)$, $g_1 = 1/2$, $g_2 = 1$, $t_0 = -10$.

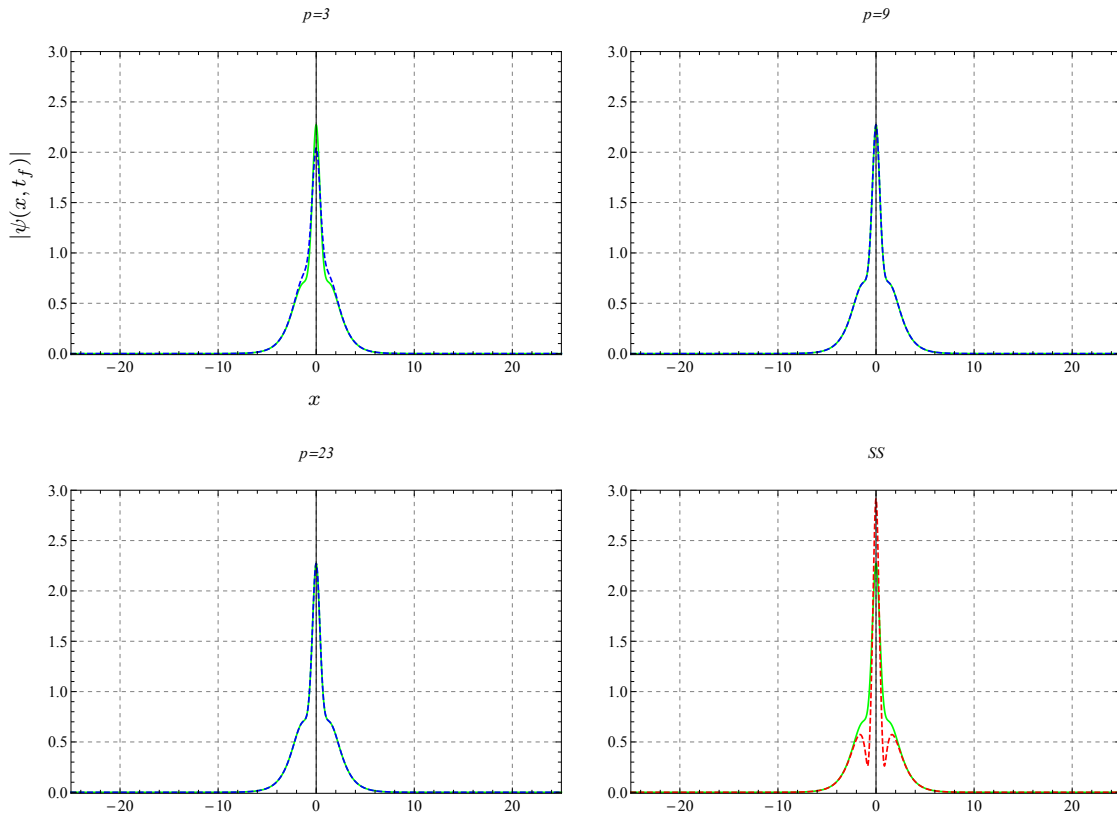


FIG. 16: Profile of the two-bright soliton solution profile at $t = 80$. Solid green curve is the analytical exact solution given by Eq.(37), dashed blue curves correspond to the present method using $p = 3, 9, 23$, and dashed red curve corresponds to the SS method. Fourth order power series expansion is used for all cases with $n_x = 4000$. The dashed red curve is the result of the SS code with $n_x = 4096$. Other parameters: $n_t = 800000$, $L = 50$, $\Delta t = 0.0001$, $t_f = n_t \times \Delta t$, $\Delta x = L/(n_x - 1)$, $g_1 = 1/2$, $g_2 = 1$, $t_0 = \phi_{01} = \phi_{02} = \nu_1 = \nu_2 = x_{01} = x_{02} = 0$, $\alpha_1 = 1$, $\alpha_2 = 2$.

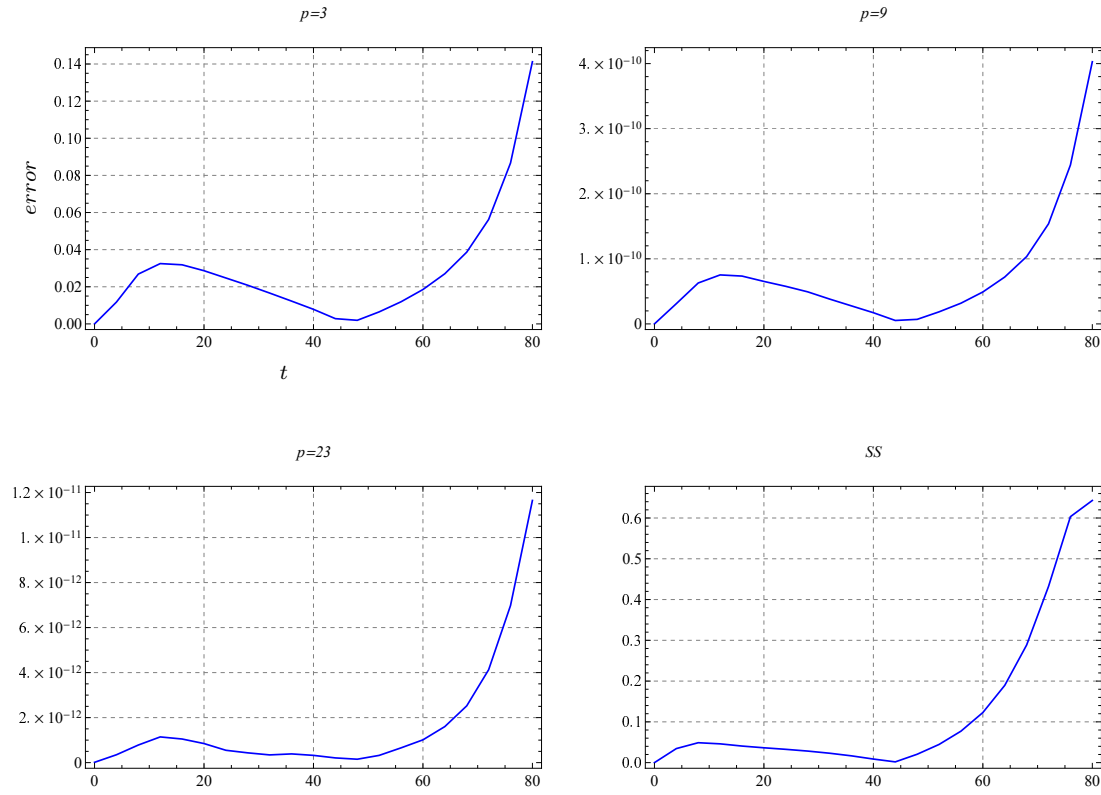


FIG. 17: Error evolution in the numerical solution of the two-bright soliton solution given by Eq. (37) using $p = 3, 9, 23$ in the second derivative discretization. Fourth order power series expansion is used for all cases. The last subfigure is the result of the SS method. Parameters used are the same as those in Fig. 16.

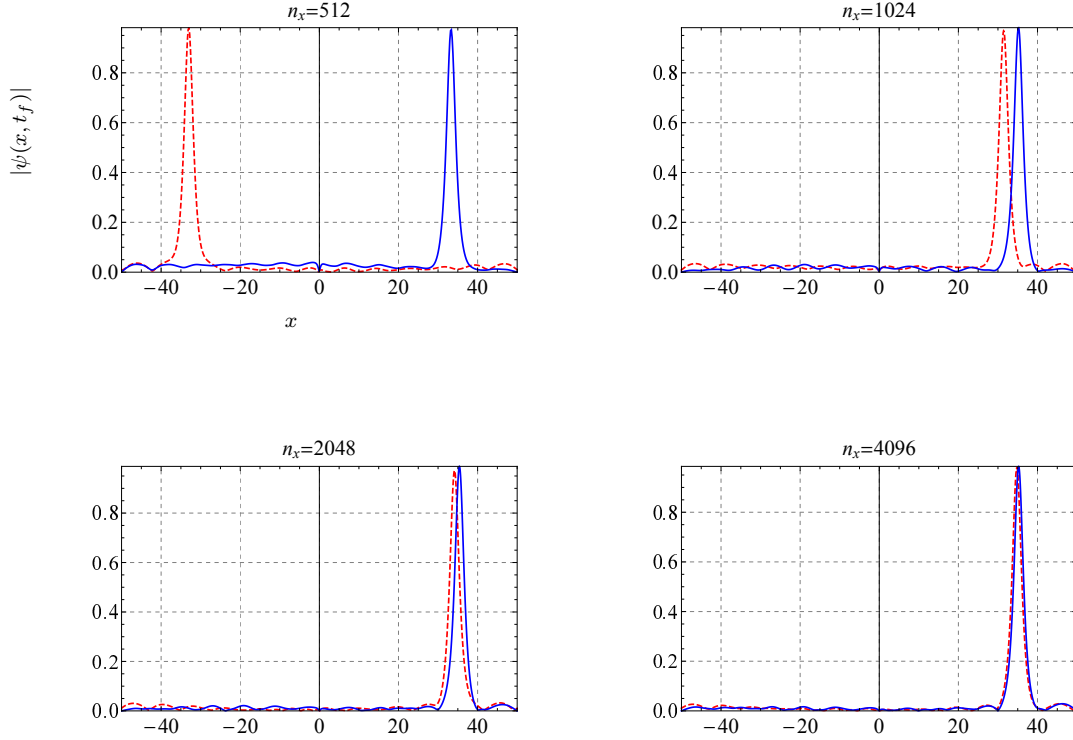


FIG. 18: Snapshot of soliton profile after scattering by the reflectionless potential (49) at $t = 153.186$. Solid blue curve corresponds to the present method and dashed red curve corresponds to the SS method. Other parameters: $\Delta t = 0.1 \times \Delta x^2$, $\Delta x = L/(n_x - 1)$, $g_1 = 1/2$, $g_2 = 1$, $x_0 = -10$, $k = 0.331$, $\alpha = 2$, $L = 100$, $p = 3$.

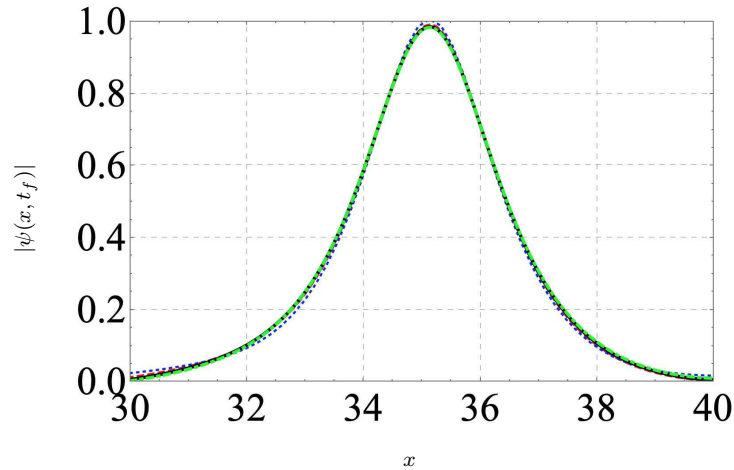


FIG. 19: Snapshot of soliton profiles obtained by the present method after scattering by the reflectionless potential (49) at $t = 153.186$. Dotted blue, dashed red, solid black, and dotted-dashed green curves correspond to $n_x = 1/2 \times 1024$, 1024 , 2×1024 , 4×1024 , respectively. Other parameters: $\Delta t = 0.1 \times \Delta x^2$, $\Delta x = L/(n_x - 1)$, $g_1 = 1/2$, $g_2 = 1$, $x_0 = -10$, $k = 0.331$, $\alpha = 2$, $p = 23$.

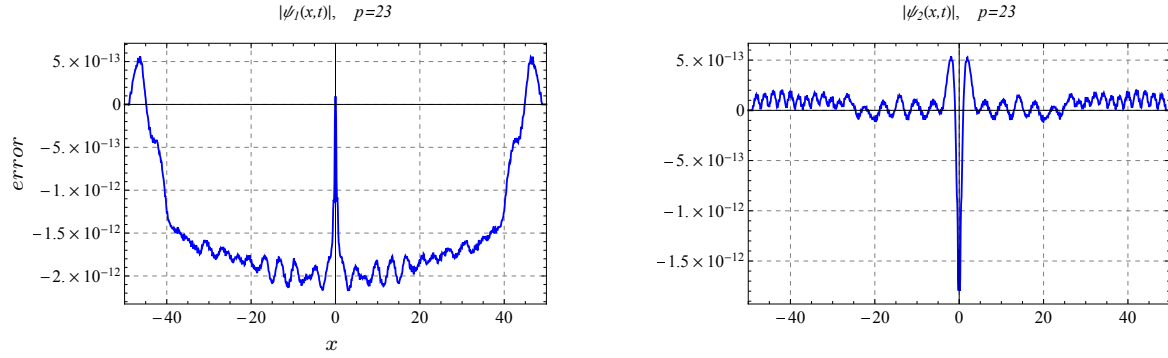


FIG. 20: Error in the numerical solution corresponding to the dark-bright soliton of the two-coupled NLSE (50) and (51) at $t = 40$ using $p = 23$ and $s = 4$. Left: Error associated with $\psi_1(x, t)$. Right: Error associated with $\psi_2(x, t)$. Parameters: $n_x = 1000$, $n_t = 80000$, $L = 100$, $\Delta t = 0.0005$, $\Delta x = L/(n_x - 1)$, $k = 0.0$, $x_0 = t_0 = 0.0$, $A_0 = 1.0$, $g_{10} = 1/2$, $g_{11} = -1$, $g_{12} = 1/2$, $g_{20} = 1/2$, $g_{21} = -1/2$, $g_{22} = 1$.

Appendix A: Deriving the p -point central difference formula of the second derivative

We first derive the p -point central difference formula that approximates a second derivative for any odd integer p . Then we present specific examples of $p = 5, \dots, 23$.

Consider the Taylor expansion

$$f(x + j\Delta x) = \sum_{i=0}^p \frac{(j\Delta x)^i}{i!} \frac{d^i f(x)}{dx^i} + \mathcal{O}\left(\frac{(j\Delta x)^{p+1}}{(p+1)!} \frac{d^{p+1} f(x)}{dx^{p+1}}\right), \quad (\text{A1})$$

and the linear combination

$$\sum_{j=1}^{(p-1)/2} C_j [f(x + j\Delta x) + f(x - j\Delta x)], \quad (\text{A2})$$

where C_j are arbitrary real coefficients. Substituting the Taylor expansion (A1) in the last expression and then exchanging the summations, it takes the form

$$\begin{aligned} & \sum_{j=1}^{(p-1)/2} C_j [f(x + j\Delta x) + f(x - j\Delta x)] \\ &= 2 \sum_{i=0}^{(p-1)/2} \left[\sum_{j=1}^{(p-1)/2} C_j \frac{(j\Delta x)^{2i}}{(2i)!} \right] \frac{df^{2i}(x)}{dx^{2i}} + \mathcal{O}\left(\frac{(j\Delta x)^{p+1}}{(p+1)!} \frac{d^{p+1} f(x)}{dx^{p+1}}\right). \end{aligned} \quad (\text{A3})$$

Requesting all coefficients of $d^{2i} f(x)/dx^{2i}$ for $i > 1$ to vanish, gives the following system of equations

$$\sum_{j=1}^{(p-1)/2} C_j \frac{(j\Delta x)^{2i}}{(2i)!} = 0 \quad (\text{A4})$$

for $i = 2, 3, \dots, (p-1)/2$. Solving (A3) for the remaining second derivative, we obtain

$$\begin{aligned} f_p'' &\equiv \frac{d^2 f(x)}{dx^2} = \frac{1}{\Delta x^2 \sum_{j=1}^{(p-1)/2} C_j j^2} \\ &\times \sum_{j=1}^{(p-1)/2} C_j [f(x + j\Delta x) + f(x - j\Delta x) - 2f(x)] \\ &+ \mathcal{O}\left(\frac{(j\Delta x)^{p+1}}{(p+1)!} \frac{d^{p+1} f(x)}{dx^{p+1}}\right), \end{aligned} \quad (\text{A5})$$

where we denote the p -point second derivative as f_p'' . The last term gives the order of error in the approximation. As an example, we take the $p = 5$ case. The system (A4) reduces to a single equation for $i = 2$, namely $c_1 + 16c_2 = 0$. Solving for c_2 and substituting back in (A5), gives the 5-point central formula as listed below.

For convenience, we calculate the p -point formulae up to $p = 23$:

$$f_5''(x) = \frac{-f(x + 2\Delta x) + 16f(x + \Delta x) - 30f(x) + 16f(x - \Delta x) - f(x - 2\Delta x)}{12\Delta x^2}, \quad (\text{A6})$$

$$f_7''(x) = \frac{1}{180\Delta x^2} \left[2f(x + 3\Delta x) - 27f(x + 2\Delta x) + 270f(x + \Delta x) - 490f(x) \right] \quad (\text{A7})$$

$$+270 f(x - \Delta x) - 27 f(x - 2 \Delta x) + 2 f(x - 3 \Delta x) \Big],$$

$$f_9''(x) = \frac{1}{5040 \Delta x^2} \Big[-9 f(x + 4 \Delta x) + 128 f(x + 3 \Delta x) - 1008 f(x + 2 \Delta x) \quad (\text{A8})$$

$$+ 8064 f(x + \Delta x) - 14350 f(x) + 8064 f(x - \Delta x) - 1008 f(x - 2 \Delta x)$$

$$+ 128 f(x - 3 \Delta x) - 9 f(x - 4 \Delta x) \Big],$$

$$f_{11}''(x) = \frac{1}{25200 \Delta x^2} \Big[8 f(x + 5 \Delta x) - 125 f(x + 4 \Delta x) + 1000 f(x + 3 \Delta x) \quad (\text{A9})$$

$$- 6000 f(x + 2 \Delta x) + 42000 f(x + \Delta x) - 73766 f(x) + 42000 f(x - \Delta x)$$

$$- 6000 f(x - 2 \Delta x) + 1000 f(x - 3 \Delta x) - 125 f(x - 4 \Delta x) + 8 f(x - 5 \Delta x) \Big],$$

$$f_{13}''(x) = \frac{1}{831600 \Delta x^2} \Big[-50 f(x + 6 \Delta x) + 864 f(x + 5 \Delta x) - 7425 f(x + 4 \Delta x) \quad (\text{A10})$$

$$+ 44000 f(x + 3 \Delta x) - 222750 f(x + 2 \Delta x) + 1425600 f(x + \Delta x) - 2480478 f(x)$$

$$+ 1425600 f(x - \Delta x) - 222750 f(x - 2 \Delta x) + 44000 f(x - 3 \Delta x)$$

$$- 7425 f(x - 4 \Delta x) + 864 f(x - 5 \Delta x) - 50 f(x - 6 \Delta x) \Big],$$

$$f_{15}''(x) = \frac{1}{75675600 \Delta x^2} \Big[900 f(x + 7 \Delta x) - 17150 f(x + 6 \Delta x) + 160524 f(x + 5 \Delta x) \quad (\text{A11})$$

$$- 1003275 f(x + 4 \Delta x) + 4904900 f(x + 3 \Delta x) - 22072050 f(x + 2 \Delta x)$$

$$+ 132432300 f(x + \Delta x) - 228812298 f(x) + 132432300 f(x - \Delta x)$$

$$- 22072050 f(x - 2 \Delta x) + 4904900 f(x - 3 \Delta x) - 1003275 f(x - 4 \Delta x)$$

$$+ 160524 f(x - 5 \Delta x) - 17150 f(x - 6 \Delta x) + 900 f(x - 7 \Delta x) \Big],$$

$$f_{17}''(x) = \frac{1}{302702400 \Delta x^2} \Big[-735 f(x + 8 \Delta x) + 15360 f(x + 7 \Delta x) \quad (\text{A12})$$

$$- 156800 f(x + 6 \Delta x) + 1053696 f(x + 5 \Delta x) - 5350800 f(x + 4 \Delta x)$$

$$+ 22830080 f(x + 3 \Delta x) - 94174080 f(x + 2 \Delta x) + 538137600 f(x + \Delta x)$$

$$- 924708642 f(x) + 538137600 f(x - \Delta x) - 94174080 f(x - 2 \Delta x)$$

$$+ 22830080 f(x - 3 \Delta x) - 5350800 f(x - 4 \Delta x) + 1053696 f(x - 5 \Delta x)$$

$$- 156800 f(x - 6 \Delta x) + 15360 f(x - 7 \Delta x) - 735 f(x - 8 \Delta x) \Big],$$

$$f_{19}''(x) = \frac{1}{15437822400 \Delta x^2} \Big[7840 f(x + 9 \Delta x) - 178605 f(x + 8 \Delta x) \quad (\text{A13})$$

$$+ 1982880 f(x + 7 \Delta x) - 14394240 f(x + 6 \Delta x) + 77728896 f(x + 5 \Delta x)$$

$$- 340063920 f(x + 4 \Delta x) + 1309875840 f(x + 3 \Delta x) - 5052378240 f(x + 2 \Delta x)$$

$$+ 27788080320 f(x + \Delta x) - 47541321542 f(x) + 27788080320 f(x - \Delta x)$$

$$- 5052378240 f(x - 2 \Delta x) + 1309875840 f(x - 3 \Delta x) - 340063920 f(x - 4 \Delta x)$$

$$+ 77728896 f(x - 5 \Delta x) - 14394240 f(x - 6 \Delta x) + 1982880 f(x - 7 \Delta x) \Big]$$

$$-178605 f(x - 8 \Delta x) + 7840 f(x + 9 \Delta x) \Big],$$

$$f''_{21}(x) = \frac{1}{293318625600 \Delta x^2} \Big[-31752 f(x + 10 \Delta x) + 784000 f(x + 9 \Delta x) \tag{A14}$$

$$-9426375 f(x + 8 \Delta x) + 73872000 f(x + 7 \Delta x) - 427329000 f(x + 6 \Delta x)$$

$$+1969132032 f(x + 5 \Delta x) - 7691922000 f(x + 4 \Delta x) + 27349056000 f(x + 3 \Delta x)$$

$$-99994986000 f(x + 2 \Delta x) + 533306592000 f(x + \Delta x) - 909151481810 f(x)$$

$$+533306592000 f(x - \Delta x) - 99994986000 f(x - 2 \Delta x) + 27349056000 f(x - 3 \Delta x)$$

$$-7691922000 f(x - 4 \Delta x) + 1969132032 f(x - 5 \Delta x) - 427329000 f(x - 6 \Delta x)$$

$$+73872000 f(x - 7 \Delta x) - 9426375 f(x - 8 \Delta x) + 784000 f(x + 9 \Delta x)$$

$$\left. -31752 f(x - 10 \Delta x) \right],$$

$$f''_{23}(x) = \frac{1}{3226504881600 \Delta x^2} \Big[75600 f(x + 11 \Delta x) - 2012472 f(x + 10 \Delta x) \tag{A15}$$

$$+26087600 f(x + 9 \Delta x) - 220114125 f(x + 8 \Delta x) + 1365606000 f(x + 7 \Delta x)$$

$$-6691469400 f(x + 6 \Delta x) + 27301195152 f(x + 5 \Delta x) - 97504268400 f(x + 4 \Delta x)$$

$$+325014228000 f(x + 3 \Delta x) - 1137549798000 f(x + 2 \Delta x) + 5915258949600 f(x + \Delta x)$$

$$-10053996959110 f(x) + 5915258949600 f(x - \Delta x) - 1137549798000 f(x - 2 \Delta x)$$

$$+325014228000 f(x - 3 \Delta x) - 97504268400 f(x - 4 \Delta x) + 27301195152 f(x - 5 \Delta x)$$

$$-6691469400 f(x - 6 \Delta x) + 1365606000 f(x - 7 \Delta x) - 220114125 f(x - 8 \Delta x)$$

$$\left. +26087600 f(x + 9 \Delta x) - 2012472 f(x - 10 \Delta x) + 75600 f(x - 11 \Delta x) \right].$$

Appendix B: Recursion relations of the two-coupled NLSE

Recursion relations for the two-coupled NLSE (54-57) up to the fourth order, $s = 4$:

$$a_1 = -g_{11} b_0^3 - b_0 [g_{11} a_0^2 + g_{12} (c_0^2 + d_0^2)] - g_{10} b_0'', \tag{B1}$$

$$a_2 = \frac{1}{2} \Big[-2g_{11} a_0 a_1 b_0 - g_{11} a_0^2 b_1 - 3g_{11} b_0^2 b_1 - g_{12} b_1 c_0^2 - g_{12} b_1 d_0^2$$

$$\left. -2g_{12} b_0 (c_0 c_1 + d_0 d_1) - g_{10} b_1'' \right], \tag{B2}$$

$$a_3 = \frac{1}{3} \Big(-g_{11} a_1^2 b_0 - 2g_{11} a_0 a_2 b_0 - 2g_{11} a_0 a_1 b_1 - 3g_{11} b_0 b_1^2 - g_{11} a_0^2 b_2 - 3g_{11} b_0^2 b_2$$

$$-g_{12} b_2 c_0^2 - 2g_{12} b_1 c_0 c_1 - g_{12} b_0 c_1^2 - 2g_{12} b_0 c_0 c_2 - g_{12} b_2 d_0^2 - 2g_{12} b_1 d_0 d_1$$

$$\left. -g_{12} b_0 d_1^2 - 2g_{12} b_0 d_0 d_2 - g_{10} b_2'' \right), \tag{B3}$$

$$a_4 = \frac{1}{4} \Big[-g_{11} b_1^3 - 2g_{11} a_0 (a_3 b_0 + a_2 b_1) - 2g_{11} a_1 (a_2 b_0 + a_0 b_2) - g_{11} a_0^2 b_3 - 3g_{11} b_0^2 b_3$$

$$-g_{12} b_3 c_0^2 - 2g_{12} b_2 c_0 c_1 - g_{12} b_1 c_1^2 - 2g_{12} b_0 c_1 c_2 - 2g_{12} b_0 c_0 c_3 - g_{12} b_3 d_0^2$$

$$-2g_{12} b_2 d_0 d_1 - 2g_{12} b_0 d_1 d_2 - 2g_{12} b_0 d_0 d_3 - g_{10} b_3''$$

$$\left. -b_1 (g_{11} a_1^2 + 6g_{11} b_0 b_2 + 2g_{12} c_0 c_2 + g_{12} d_1^2 + 2g_{12} d_0 d_2) \right] \tag{B4}$$

$$b_1 = g_{11} a_0^3 + a_0 [g_{11} b_0^2 + g_{12} (c_0^2 + d_0^2)] + g_{10} a_0'', \tag{B5}$$

$$b_2 = \frac{1}{2} \Big\{ 3g_{11} a_0^2 a_1 + a_1 [g_{11} b_0^2 + g_{12} (c_0^2 + d_0^2)] + 2a_0 (g_{11} b_0 + g_{12} c_0 c_1 + g_{12} d_0 d_1) \Big\}$$

$$+g_{10} a_1'' \}, \quad (\text{B6})$$

$$b_3 = \frac{1}{3} \left\{ 3g_{11} a_0^2 + 2g_{11} a_1 b_0 b_1 + 2g_{12} a_1 c_0 c_1 + a_2 [g_{11} b_0^2 + g_{12} (c_0^2 + d_0^2)] + 2g_{12} a_1 d_0 d_1 \right. \\ \left. + a_0 (3g_{11} a_1^2 + g_{11} b_1^2 + 2g_{11} b_0 b_2 + g_{12} c_1^2 + 2g_{12} c_0 c_2 + g_{12} d_0 d_2) + g_{10} a_2'' \right\}, \quad (\text{B7})$$

$$b_4 = \frac{1}{4} \left\{ g_{11} a_1^3 + 3g_{11} a_0^2 a_3 + g_{11} a_3 b_0^2 + 2g_{11} a_2 b_0 b_1 + g_{12} a_3 c_0^2 \right. \\ \left. + 2g_{12} a_2 c_0 c_1 + g_{12} a_3 d_0^2 + 2g_{12} a_2 d_0 d_1 + g_{10} a_3'' \right. \\ \left. + a_1 (6g_{11} a_0 a_2 + g_{11} b_1^2 + 2g_{11} b_0 b_2 + g_{12} c_1^2 + 2g_{12} c_0 c_2 + g_{12} d_1^2 + 2g_{12} d_0 d_2) \right. \\ \left. + 2a_0 [g_{11} b_1 b_2 + g_{11} b_0 b_3 + g_{12} (c_1 c_2 + c_0 c_3 + d_1 d_2 + d_0 d_3)] \right\}, \quad (\text{B8})$$

$$c_1 = -g_{21} a_0^2 d_0 - g_{21} b_0^2 d_0 - g_{22} c_0^2 d_0 - g_{22} d_0^3 - g_{20} d_0'', \quad (\text{B9})$$

$$c_2 = \frac{1}{2} \left(-2g_{21} a_0 a_1 d_0 - 2g_{21} b_0 b_1 d_0 - 2g_{22} c_0 c_1 d_0 - g_{21} a_0^2 d_1 - g_{21} b_0^2 d_1 - g_{22} c_0^2 d_1 \right. \\ \left. - 3g_{22} d_0^2 d_1 - g_{20} d_1'' \right), \quad (\text{B10})$$

$$c_3 = \frac{1}{3} \left(-g_{21} a_1^2 d_0 - 2g_{21} a_0 a_2 d_0 - g_{21} b_1^2 d_0 - 2g_{21} b_0 b_2 d_0 - g_{22} c_1^2 d_0 - 2g_{22} c_0 c_2 d_0 \right. \\ \left. - 2g_{21} a_0 a_1 d_1 - 2g_{21} b_0 b_1 d_1 - 2g_{22} c_0 c_1 d_1 - 3g_{22} d_0 d_1^2 - g_{21} a_0^2 d_2 - g_{21} b_0^2 d_2 \right. \\ \left. - g_{22} c_0^2 d_2 - 3g_{22} d_0^2 d_2 - g_{20} d_2'' \right), \quad (\text{B11})$$

$$c_4 = \frac{1}{4} \left[-2g_{21} b_1 b_2 d_0 - 2g_{21} b_0 b_3 d_0 - 2g_{22} c_1 c_2 d_0 - 2g_{22} c_0 c_3 d_0 - g_{21} a_1^2 d_1 - g_{21} b_1^2 d_1 \right. \\ \left. - 2g_{21} b_0 b_2 d_1 - g_{22} c_1^2 d_1 - 2g_{22} c_0 c_2 d_1 - g_{22} d_1^3 - 2g_{21} a_0 (a_3 d_0 + a_2 d_1) \right. \\ \left. - 2g_{21} b_0 b_1 d_2 - 2g_{22} c_0 c_1 d_2 - 6g_{22} d_0 d_1 d_2 - 2g_{21} a_1 (a_2 d_0 + a_0 d_2) - g_{21} a_0^2 d_3 \right. \\ \left. - g_{21} b_0^2 d_3 - g_{22} c_0^2 d_3 - 3d_0^2 d_3 - g_{20} d_3'' \right], \quad (\text{B12})$$

$$d_1 = g_{21} a_0^2 c_0 + g_{21} b_0^2 c_0 + g_{22} c_0 d_0^2 + g_{22} c_0^3 + g_{20} c_0'', \quad (\text{B13})$$

$$d_2 = \frac{1}{2} \left(2g_{21} a_0 a_1 c_0 + 2g_{21} b_0 b_1 c_0 + 2g_{22} c_0 d_0 d_1 + g_{21} a_0^2 c_1 + g_{21} b_0^2 c_1 + g_{22} d_0^2 c_1 \right. \\ \left. + 3g_{22} c_0^2 c_1 + g_{20} c_1'' \right), \quad (\text{B14})$$

$$d_3 = \frac{1}{3} \left(g_{21} a_1^2 c_0 + 2g_{21} a_0 a_2 c_0 + g_{21} b_1^2 c_0 + 2g_{21} b_0 b_2 c_0 + 2g_{21} a_0 a_1 c_1 + 2g_{21} b_0 b_1 c_1 \right. \\ \left. + 3g_{22} c_0 c_1^2 + g_{21} a_0^2 c_2 + g_{21} b_0^2 c_2 + 3g_{22} c_0^2 c_2 + g_{22} c_2 d_0^2 + 2g_{22} c_1 d_0 d_1 \right. \\ \left. + g_{22} c_0 d_1^2 + 2g_{22} c_0 d_0 d_2 + g_{20} c_2'' \right), \quad (\text{B15})$$

$$d_4 = \frac{1}{4} \left[2g_{21} b_1 b_2 c_0 + 2g_{21} b_0 b_3 c_0 + g_{21} a_1^2 c_1 + g_{21} b_1^2 c_1 + 2g_{21} b_0 b_2 c_1 + g_{22} c_1^3 \right. \\ \left. + 2g_{21} a_0 (a_3 c_0 + a_2 c_1) + 2g_{21} b_0 b_1 c_2 + 6g_{22} c_0 c_1 c_2 + 2g_{21} a_1 (a_2 c_0 + a_0 c_2) \right. \\ \left. + g_{21} a_0^2 c_3 + g_{21} b_0^2 c_3 + 3g_{22} c_0^2 c_3 + g_{22} c_3 d_0^2 + 2g_{22} c_2 d_0 d_1 + g_{22} c_1 d_1^2 \right. \\ \left. + 2g_{22} c_1 d_0 d_2 + 2g_{22} c_0 d_1 d_2 + 2g_{22} c_0 d_0 d_3 + g_{20} c_3'' \right]. \quad (\text{B16})$$

[1] C. J. Pethick and H. Smith, "Bose-Einstein Condensation in Dilute Gases", Cambridge, Cambridge University Press, 2008.

- [2] A. Hasegawa and Y. Kodama, “Solitons in optical communications”, Oxford: Oxford Univ. Press, (1995); C. Sulem, P.-L. Sulem, “The Nonlinear Schrödinger Equation: Self-Focusing and Wave Collapse”, in: Applied Mathematical Sciences, **139**, Springer-Verlag, New York, 1999; L. Mollenauer and J. Gordon, “Solitons in optical fibers”, Boston: Academic Press, 2006; N. Akhmediev and A. Ankiewicz, “Solitons: Nonlinear Pulses and Beams”, London: Chapman and Hall, 1997; G. Agrawal, “Nonlinear fiber optics”, 3rd ed, San Diego: Academic Press, 2001; Y. S. Kivshar and G. P. Agrawal, “Optical Solitons”. Academic Press, San Diego, 2003.
- [3] C. Kharif, E. Pelinovsky, A. Slyunyaev, “Rogue waves in the ocean”, Berlin: Springer, 2009.
- [4] P. AO, D. J. Thouless, and X.-M. Zhu, “Nonlinear Schrödinger equation for superconductors”, Modern Physics Letters B **09**, 755-761 (1995).
- [5] S. F. Mingaleev, P. L. Christiansen, Y. B. Gaididei, M. Johansson, and K. Ø. Rasmussen, “Models for energy and charge transport and storage in biomolecules”, J. Biol. Phys. **25**, 41-63 (1999).
- [6] Y. Shi and J. E. Hearst, “The kirchhoff elastic rod, the nonlinear Schrödinger equation, and DNA supercoiling”, J. Chem. Phys. **101**, 5186-5200 (1994).
- [7] U. Al Khawaja and L. Al Sakkaf, “Handbook of Exact Solutions to the Nonlinear Schrödinger Equations”, (IOP publishing, London 2019).
- [8] X. Antoine, W. Bao, C. Besse, “Computational methods for the dynamics of the nonlinear Schrödinger/Gross-Pitaevskii equations”, Computer Physics Communications **184** 2621-2633 (2013).
- [9] F. I. Moxley III, D. T. Chuss, W. Dai, “A generalized finite-difference time-domain scheme for solving nonlinear Schrödinger equations,” Computer Physics Communications **184**, 1834-1841 (2013).
- [10] W. Bao, Q. Tang, Z. Xu, “Numerical methods and comparison for computing dark and bright solitons in the nonlinear Schrödinger equation”, Journal of Computational Physics **235**, 423-445 (2013).
- [11] J.A.C. Weideman, B.M. Herbst, “Split-step methods for the solution of the nonlinear Schrödinger equation”, SIAM Journal on Numerical Analysis **23**, 485-507 (1986).
- [12] J. Ming, Q. Tang, Y. Zhang, “An efficient spectral method for computing dynamics of rotating two-component Bose-Einstein condensates via coordinate transformation”, Journal of Computational Physics **258**, 538-554 (2014).
- [13] Mohammad S Ismail, K. S. Al-Basyouni and A. Aydin, “Conservative finite difference schemes for the chiral nonlinear Schrödinger equation”, Boundary Value Problems **89**, 2015 (2015).
- [14] Ph. Mocz and S. Succi, “Numerical solution of the nonlinear Schrödinger equation using smoothed-particle hydrodynamics”, Phys. Rev. E **91**, 053304 (2015).
- [15] M. Dehghan, V. Mohammadi, “A numerical scheme based on radial basis function finite difference (RBF-FD) technique for solving the high-dimensional nonlinear Schrödinger equations using an explicit time discretization: Runge-Kutta method,” Computer Physics Communications **217**, 23-34 (2017).
- [16] T. Jiang, Zhen-Chao Chen, Wei-Gang Lu, Jin-Yun Yuan, Deng-Shan Wang, “An efficient split-step and implicit pure mesh-free method for the 2D/3D nonlinear Gross-Pitaevskii equations”, Computer Physics Communications **231**, 19-30 (2018).
- [17] J. Wang, X. Liu, Y. Zhou, “A high-order accurate wavelet method for solving Schrödinger equations with general nonlinearity”, Appl. Math. Mech. -Engl. Ed., **39**, 275-290 (2018).
- [18] J. P. Wilson, Generalized Finite-Difference “Time-Domain method with absorbing boundary conditions for solving the nonlinear Schrödinger equation on a GPU”, Computer Physics Communications **235**, 279-292 (2019).
- [19] L. Kong, P. Wei, Y. Hong, P. Zhang, and P. Wang, “Efficient energy-preserving scheme of the three-coupled nonlinear Schrödinger equation”, Math. Meth. Appl. Sci. **42**, 3222-3235 (2019).
- [20] B.D. Shizgal, H. Chen, “The quadrature discretization method (QDM) in the solution of the Schrödinger equation with nonclassical basis functions”, J. Chem. Phys. **104**, 4137-4150 (1996).
- [21] K. Leung, B. D. Shizgal, H. Chen, “The quadrature discretization method (QDM) in comparison with other numerical methods of solution of the Fokker-Planck equation for electron thermalization”, J. Math. Chem. **24**, 291-319 (1998).
- [22] H. Chen, B. D. Shizgal, “The quadrature discretization method (QDM) in the solution of the Schrödinger equation”, J. Math. Chem. **24**, 321-343 (1998).
- [23] J. Lo, B. D. Shizgal, “Spectral convergence of the quadrature discretization method in the solution of the Schrödinger and Fokker-Planck equations: comparison with sinc methods”, J. Chem. Phys. **125**, 194108 (2006).
- [24] U. Al Khawaja, Q. M. Al-Mdallal, “Convergent Power Series of and Solutions to Nonlinear Differential

- Equations”, *International Journal of Differential Equations*, **2018**, 6043936 (2018).
- [25] LY Al Sakkaf, Q. M. Al-Mdallal, and U. Al Khawaja, “A Numerical algorithm for solving higher-order nonlinear BVPs with an application on fluid flow over a shrinking permeable infinite long cylinder”, *Complexity* **2018**, 8269541 (2018).
- [26] F. I. Moxley III, “Generalized finite-difference time-domain schemes for solving nonlinear Schrödinger equations”, *Doctoral Dissertations, Louisiana Tech University Louisiana Tech Digital Commons*, 2013.
- [27] R. H. Goodman, P. J. Holmes, and M. I. Weinstein, “Strong NLS soliton-defect interactions”, *Physica D*, **192**, 215-248 (2004).
- [28] C. Lee and J. Brand, “Enhanced quantum reflection of matter-wave solitons”, *Europhys. Lett.*, **73**, 321-327 (2006).
- [29] T. Ernst and J. Brand, “Resonant trapping in the transport of a matter-wave soliton through a quantum well”, *Phys. Rev. A.*, **81**, 033614 (2010).